



**UNIVERSIDAD DE INVESTIGACIÓN DE
TECNOLOGÍA EXPERIMENTAL YACHAY**

Escuela de Ciencias Químicas e Ingeniería

TÍTULO:
**First-Principles Analysis of Electronic and Optical
Properties of Selected Na-Sb Phases**

Trabajo de integración curricular presentado como requisito para la
obtención de título de Química

Autor:

Rubio Apolo Cristina
Stefania

Tutor:

Terencio Thibault, Ph.D.

Co-tutor:

Cocchi Caterina, Ph.D.

Urcuquí, abril 2024

AUTORÍA

Yo, **RUBIO APOLO CRISTINA STEFANIA**, con cédula de identidad 1725661266, declaro que las ideas, juicios, valoraciones, interpretaciones, consultas bibliográficas, definiciones y conceptualizaciones expuestas en el presente trabajo; así como, los procedimientos y herramientas utilizadas en la investigación, son de absoluta responsabilidad de el/la autor (a) del trabajo de integración curricular. Así mismo, me acojo a los reglamentos internos de la Universidad de Investigación de Tecnología Experimental Yachay.

Urcuquí, abril 2024

Cristina Stefania Rubio Apolo
CI: 1725661266

AUTORIZACIÓN DE PUBLICACIÓN

Yo, **RUBIO APOLO CRISTINA STEFANIA**, con cédula de identidad 1725661266, cedo a la Universidad de Investigación de Tecnología Experimental Yachay, los derechos de publicación de la presente obra, sin que deba haber un reconocimiento económico por este concepto. Declaro además que el texto del presente trabajo de titulación no podrá ser cedido a ninguna empresa editorial para su publicación u otros fines, sin contar previamente con la autorización escrita de la Universidad.

Asimismo, autorizo a la Universidad que realice la digitalización y publicación de este trabajo de integración curricular en el repositorio virtual, de conformidad a lo dispuesto en el Art. 144 de la Ley Orgánica de Educación Superior.

Urcuquí, abril 2024.

Cristina Stefania Rubio Apolo

CI: 1725661266

Dedication

To those who dare to dream even in their darkest days.

Cristina Rubio

Acknowledgements

I am immensely grateful to Dr. Caterina and Holger for welcoming me into their research group. Moreover, I extend my heartfelt thanks to the University of Oldenburg for facilitating my access to the HPC Carl supercomputer, which is fundamental to performing the present work. I am filled with immense gratitude towards Prof. Thibault for his constant support, unshakeable belief in me, and encouragement to pursue even my most crazy ideas. His remarkable patience with my progress has been truly exceptional. I hope his passion for science and life continues to inspire countless young minds. He has instilled in me a love for learning, a drive to explore new ideas, and a desire to make a positive impact on the world around me. I feel incredibly fortunate to have had the opportunity to work with him, and I am confident that his influence will continue to shape my life for years to come. To Prof. Manuel, Lolita, Antonio, Vivian, Floralba, Sandra, and Mariela, your guidance and support have been invaluable, providing me with the knowledge, skills, and resources I need to succeed. The opportunities you have provided me with have been crucial to my growth and development, allowing me to achieve my skills and gain valuable experience. Each and every one of you holds a special place in my heart, and I am forever indebted to you for your unwavering commitment to my success.

I would like to express my deepest gratitude to my beloved mother, Paty. Throughout my life, she has been my constant support system, providing me with love, guidance, and encouragement every step of the way. I owe all my successes to her tireless efforts, and I am forever grateful for her presence in my life. My father, Christian, has been an equally important role model in my life. He has instilled in me the values of discipline, hard work, determination, and a love for good music and science. He has always pushed me to be my best and never settle for anything less. He has been a constant source of inspiration and motivation. To my beautiful and smart sisters, Erika and Martina, I owe an immeasurable debt of gratitude. They have been my closest confidantes and greatest motivators. They have always been there for me, offering their love, support, and guidance. Together, we form an indomitable force capable of conquering any challenge that comes our way.

To Milene and Mafer, I express my deepest gratitude for your support and friendship. Your presence through life's highs and lows has provided me with motivation and strength beyond measure. To my dear friends, Ema, Alejo, and Elian, your unconditional love, unwavering support, and complete acceptance have been a blessing of light in my darkest moments. I am truly grateful to have you all in my life.

And to Melany, Alexis, Paula and Dani, I extend my heartfelt thanks for your friendship and presence during both the trials and triumphs of life. Your generosity, kindness, and warm embraces have meant more to me than words can express. Your friendship means the world to me, and I am truly blessed to have you all in my life.

My dearest Ariel, I want to express my gratitude for the support and inspiration you have provided me with. Your love for me has been an unyielding source of strength and motivation, allowing me to break through barriers and achieve my full potential. I cannot imagine where I would be today without your encouragement and guidance. You have been my rock during difficult times, always there to provide comfort, guidance, and reassurance. Your unwavering belief in me has given me the courage to pursue my dreams and overcome obstacles that once seemed impossible. If love could be defined, it would bear your name. Your love is selfless, pure, and unconditional. You have profoundly impacted my life in ways I never thought possible, and for that, I am forever grateful. I want you to know that I appreciate everything you have done for me, and no amount of words could adequately convey the depth of my gratitude. You are my everything, and I am incredibly lucky to have you in my life.

Cristina

Resumen

El desarrollo de haces de electrones ultrabrillantes en los modernos aceleradores de partículas está impulsando nuevas técnicas experimentales. Los nuevos materiales de fotocátodos pueden contribuir significativamente a mejorar estas instalaciones. El proyecto tiene como objetivo desarrollar nuevos materiales para fuentes de electrones de vacío en aceleradores de partículas, que es un campo de investigación activo. Los cálculos *ab initio* pueden predecir la estructura electrónica de los sistemas objetivo, pero los cálculos de la teoría de perturbaciones de muchos cuerpos son demasiado costosos para la detección de materiales a gran escala. La teoría del funcional de densidad ofrece el mejor compromiso entre precisión y viabilidad computacional. En este proyecto, se caracterizará la estructura electrónica de las fases de antimonuro de sodio, que es una clase emergente de semiconductores explorados como material de fotocátodo. Se utilizarán diferentes estructuras cristalinas con diferentes composiciones como entrada para acceder a los estados y valores propios electrónicos. Esto ayudará a identificar los cambios relevantes en las propiedades electrónicas y ópticas con respecto a diferentes estructuras y estequiometrías. Se inspeccionará la estructura de bandas y la densidad de estados (DOS), que se descompone aún más en contribuciones proyectadas por átomos. Nuestros resultados muestran que el funcional SCAN es una excelente opción en términos de precisión y eficiencia computacional y una mejora general del funcional PBE y HSE06. Finalmente, se evaluará el desempeño de los tres funcionales antes mencionados en la descripción de los efectos del acoplamiento espín-órbita (SOC), que se sabe que son relevantes en los materiales investigados, ya que están compuestos por especies atómicas relativamente pesadas.

Palabras clave: Antimonuros-multialcalinos, Teoría del Funcional de Densidad, Funcional de Intercambio-Correlación.

Abstract

Developing ultra-bright electron beams in modern particle accelerators is driving new experimental techniques. Novel photocathode materials can significantly contribute to improving these facilities. The project aims to develop new materials for vacuum electron sources in particle accelerators, an active research field. Ab initio calculations can predict the electronic structure of target systems, but many-body perturbation theory calculations are too costly for large-scale material screening. Regarding accuracy and computational feasibility, density functional theory is the top choice. This project will characterize the electronic structure of sodium-antimonide phases, and an emerging semiconductor class will be explored as photocathode material. Different crystal structures with varying compositions will be used as input to access the electronic eigenstates and eigenvalues. This will help identify the relevant changes in the electronic and optical properties concerning different structures and stoichiometries. We will examine the band structure and density of states (DOS), which can be separated into atom-projected contributions. Our findings indicate that the SCAN functional is highly suitable for precision, computational speed, and overall enhancement compared to the PBE and HSE06 functional. At last, we will evaluate how well the three functionals mentioned earlier capture the spin-orbit coupling (SOC) effects in the materials we are studying. These effects are important because the materials contain heavy atoms.

Keywords: multi-alkali antimonides, density-functional theory, exchange-correlation functional.

Contents

Acknowledgements	ix
Resumen	xi
Abstract	xiii
List of Figures	xvii
List of Tables	xxi
1 Background	1
1.1 Introduction	1
1.2 Problem Statement	2
1.3 General and Specific Objectives	3
1.3.1 General Objective	3
1.3.2 Specific Objectives	3
2 Theoretical Framework	5
2.1 The Many-body Problem in Quantum Mechanics	5
2.1.1 Density Functional Theory (DFT) principles	8
2.1.1.1 The Hohenberg-Kohn Theorem	8
2.1.1.2 The Kohn-Sham equation	9
2.1.2 Exchange-correlation functional E_{xc}	10
2.1.2.1 The Local Spin Density Approximation (LSDA)	11
2.1.2.2 The generalized gradient approximation (GGA)	12
2.1.2.3 The PBE functional	12
2.1.2.4 The SCAN functional	13
2.1.2.5 The HSE06 functional	14
2.2 Ultra-bright Electron Beams	14
2.3 Photocathode Materials	15
2.3.1 Mono- and bi-alkali antimonides	16

3	Methodology	21
3.1	Computational Details	21
3.2	Workflow	23
3.2.1	Self Consistent Field Calculations	24
3.2.2	Convergency k-points and Cell Optimization	24
3.2.3	Band Structure and Density of States	25
3.2.4	Dielectric Function Calculations	26
3.2.5	Core-Level Spectroscopy Calculations	27
3.2.6	Spin Orbital Coupling Calculations	28
4	Results and Discussion	29
4.1	Structural Parameters	29
4.1.1	Cell Optimization	29
4.2	Electronic Properties	32
4.2.1	Band Structure and Density of States	32
4.2.2	Spin Orbital Coupling Effect	38
4.3	Optical Properties	40
4.3.1	Dielectric Function	40
4.3.1.1	Elemental Phases	40
4.3.1.2	Multi-Alkali Antimonides	44
4.4	Core-Level Spectroscopy	48
5	Conclusions and future work	53
6	Annexes	55
6.1	Band Structures and DOS	55
	Bibliography	59

List of Figures

3.1	Workflow developed in the present work.	22
3.2	DFT workflow applied in order to elucidate the electronic and optical properties of the materials proposed in the present work.	24
4.1	Ball and stick representation of the primitive unit cells of (a) Na, (b) Sb, and (c) K. Plots produced with the visualization software XCrysDen ⁸²	30
4.2	Ball and stick representation of the primitive unit cells of (a) Na ₃ Sb, (b) Na ₂ KSb, and (c) NaK ₂ Sb. Plots produced with the visualization software XCrysDen ⁸²	30
4.3	Illustrated in the graphics are the high-symmetry points and the path connecting them in the Brillouin zones of Na, Sb, and K. These graphics were created using XCrysDen	33
4.4	Band structure and PDOS of elemental phases (a) Na, (b) Sb, and (c) K using SCAN functional. The energy is referenced to the valence band maximum with a dashed line.	34
4.5	Illustrated in the graphics are the high-symmetry points and the path connecting them in the Brillouin zones of Na ₃ Sb and Na ₂ KSb. These visuals were created using XCrysDen ⁸²	35
4.6	Band structure and PDOS of the different bulks: (a) Na ₃ Sb, (b) Na ₂ KSb, and (c) NaK ₂ Sb using SCAN functional. The energy is referenced to the valence band maximum with a dashed line.	36
4.7	Computed band structures of Na using (a) PBE, (b) SCAN, and (c) HSE06 functionals with and without SOC. The valence band maxima without SOC correction are set to zero. Solid and dashed lines represent with and without SOC, respectively.	38
4.8	Computed band structures of Sb using (a) PBE, (b) SCAN, and (c) HSE06 functionals with and without SOC. The valence band maxima without SOC correction are set to zero. Blue solid and orange dashed lines represent with and without SOC, respectively.	39

4.9	Computed band structures of Na ₃ Sb using (a) PBE, (b) SCAN, and (c) HSE06 functionals with and without SOC. The valence band maxima without SOC correction are set to zero. Blue solid and orange dashed lines represent with and without SOC, respectively.	39
4.10	Computed band structures of (a) K, (b) NaK ₂ Sb, and (c) Na ₂ KSb. The valence band maxima without SOC correction are set to zero. Blue solid and orange dashed lines represent with and without SOC, respectively.	40
4.11	Imaginary and real part of the dielectric functions corresponding to Na with different functionals: (a) PBE, (b) SCAN, and (c) HSE06. . .	42
4.12	Imaginary and real part of the dielectric functions corresponding to Sb with different functionals: (a) PBE, (b) SCAN, and (c) HSE06. . . .	43
4.13	Imaginary and real part of the dielectric functions corresponding to K using SCAN as functional.	44
4.14	Imaginary and real part of the dielectric functions corresponding to Na ₃ Sb with different functionals: (a) PBE, (b) SCAN, and (c) HSE06. . . .	46
4.15	Imaginary and real part of the dielectric functions corresponding to Na ₂ KSb using SCAN functional.	47
4.16	Imaginary and real part of the dielectric functions corresponding to NaK ₂ Sb using SCAN functional.	47
4.17	Ball and stick representation from different perspectives of the primitive unit cells of Na ₃ Sb, Na (A ₁) atoms in blue light, Na (A ₂) atoms in green, and Sb atoms in grey. Plots produced with the visualization software XCrysDen ⁸²	49
6.1	Na's band structure and PDOS were obtained using different functionals: PBE, SCAN, and HSE06. The energy is referenced to the valence band maximum (dashed line).	55
6.2	Comparison of Sb's band structure and PDOS using three different functional methods: PBE, SCAN, and HSE06. The valence band maximum is marked as the zero energy level with a dashed line.	56
6.3	The band structure and partial density of states (PDOS) of Na ₃ Sb were determined using three different functional methods: PBE, SCAN, and HSE06. The zero energy level is marked by a dashed line, representing the valence band maximum. The contribution from various orbitals (s, p, d, and f) is depicted by solid, dashed, dotted, and dash-dotted lines, respectively.	57

6.4	Comparison of Sb's band structure and PDOS using three different functional methods: PBE, SCAN, and HSE06. The valence band maximum is marked as the zero energy level with a dashed line.	58
-----	--	----

List of Tables

2.1	Comparison of photocathode materials (Part 1)	18
2.2	Comparison of photocathode materials (Part 2)	19
3.1	Data used for the generation of inputs used in Jupyter.	23
3.2	Highlighted Grid Convergence: In this table, all checked grids are displayed, with the converged ones emphasized in bold for easy identification.	25
4.1	Lattice parameters, volume per atom (Ω), and formation energy per atom (E_{for}) of the conventional unit cell of Na, Sb and Na ₃ Sb	31
4.2	Lattice parameters, volume per atom (Ω), and formation energy per atom (E_{for}) of the conventional unit cell of K, NaK ₂ Sb, and Na ₂ KSb.	32
4.3	Electronic gaps including SOC effect corresponding to Na, Sb, Na ₃ Sb in eV.	37
4.4	Electronic gaps including SOC effect corresponding to K, Na ₂ KSb, NaK ₂ Sb in eV.	38
4.5	Core-level binding energies computed from DFT for 1s-orbital in Na ₃ Sb, Na ₂ KSb, and NaK ₂ Sb. Inequivalent Na atoms are identified based on their crystallographic sites. All values are expressed in electronvolts (eV).	49
4.6	Core-level binding energies computed from DFT for 2s-orbital in Na ₃ Sb, Na ₂ KSb, and NaK ₂ Sb. All values are expressed in electronvolts (eV).	49
4.7	Core-level binding energies computed from DFT for 3s-orbital in Na ₃ Sb, Na ₂ KSb, and NaK ₂ Sb. All values are expressed in electronvolts (eV).	50
4.8	Core-level binding energies computed from DFT for 2p-orbital in Na ₃ Sb, Na ₂ KSb, and NaK ₂ Sb. All values are expressed in electronvolts (eV).	50
4.9	Core-level binding energies computed from DFT for 3p-orbital in Na ₃ Sb, Na ₂ KSb, and NaK ₂ Sb.	50
4.10	Core-level binding energies computed from DFT for Sb core levels orbital in Na ₃ Sb, Na ₂ KSb, and NaK ₂ Sb. All values are expressed in electronvolts (eV).	51

Chapter 1

Background

1.1 Introduction

Mono- and bi-alkali antimonides, represented by X_2YSb (where X and Y are from Group I), have the potential to generate high-quality electron beams in the next generation of electronic devices. This is due to their intrinsic high quantum efficiency in the visible region of the spectrum. These antimonides have shown great performance as electron sources in current photoinjectors. They have a relatively tiny band gap of around 1 eV and an electron affinity of about 1 eV. This results in threshold emission in the visible or near-infrared spectrum while also displaying high quantum efficiencies equivalent to classic photocathodes, like GaAs¹⁻⁶. Recent research has demonstrated that alkali antimonides can be produced as polycrystals with extremely smooth surfaces. However, most photocathodes utilized in photoinjectors have disordered structures and lack long-range organization. Experimental investigations into the structural and optoelectronic properties of single-crystal versions of these materials are particularly difficult due to their great sensitivity to vacuum conditions and the requirement for ultra-high vacuum to survive only in thin film forms.

To investigate the problem, we thoroughly examined the stability of single-crystal mono- and bi-alkali antimonides from scratch. However, our results' accuracy significantly depends on the exchange-correlation potential, indicated as v_{xc} . To guarantee the trustworthiness of our findings, we exhaustively analyzed three popular approximations of v_{xc} : PBE, SCAN, and HSE06. These approximations are classified into three types (GGA, meta-GGA, and hybrids) commonly used in solids research.

We investigated three significant compounds: mono- and bi-alkali antimonides (Na_3Sb , NaK_2Sb , and Na_2KSb) and their elemental phases, which have applications in photoemission and photoabsorption. Our investigation includes optimizing the

lattice parameters and comparing the results to experimental values. We also calculated band structure, density of states (DOS), dielectric constants, and core spectroscopy better to understand these compounds' electrical and optical properties. Our investigation found that the SCAN function is more accurate and efficient than the PBE and HSE06 functionals. We also explored the influence of spin-orbital coupling (SOC) on the electronic structure, which has a major impact on the optical absorption edge location. Our findings indicate that SOC minimizes these materials' electrical characteristics and is equally captured by all v_{xc} estimates.

1.2 Problem Statement

Electron sources are important in contemporary technology, including microscopes, radio transmitters, and X-ray tubes in medical diagnostic instruments. The process of accelerating electrons in a particle accelerator has resulted in the development of numerous applications. Therefore, enhancing the development of superior electron sources for basic and applied research is crucial. Enhancements are needed for the current electron sources to fulfill the requirements of increased electron currents, elevated repetition rates, and beams with high brightness. Modern photoinjectors significantly depend on the inherent emittance at the photocathode to provide optimal electron beam performance.

Further progress in this field requires substantial enhancements in electron sources. Throughout history, copper has been widely used for building photocathodes because of its high carrier density, which facilitates efficient electrical charge transfer, and its low work function, which enables the emission of electrons with minimal energy input. Nevertheless, these materials are not suited for the upcoming generation of electron sources due to their propensity to absorb UV radiation, necessitating costly frequency conversion, and their tendency to generate heat, leading to inefficiencies. Hence, in the past ten years, a novel type of semiconductor material known as multi-alkali antimonides has surfaced as a promising material for photocathodes. Their efficacy in electron emission devices mostly stems from their strong photon absorption and favorable work function properties. Additional data regarding their electronic and optical properties is required to enhance comprehension of the electronic mechanisms involved in utilizing these materials.

1.3 General and Specific Objectives

1.3.1 General Objective

This research project aims to comprehensively examine the structural and optoelectronic characteristics of single-crystal mono- and bi-alkali antimonides. The study will largely assess their stability by employing different exchange-correlation potentials. This research aims to offer useful insights into the prospective uses of these antimonides, namely in electrical systems that necessitate high-quality electron beams.

1.3.2 Specific Objectives

- Assess the accuracy and reliability of three frequently employed exchange-correlation potentials - PBE, SCAN, and HSE06 - in predicting the stability and electrical properties of single-crystal mono- and bi-alkali antimonides. Considering the materials' extreme sensitivity to vacuum conditions, a thorough evaluation of their appropriateness is necessary.
- Conduct a comprehensive optimization of lattice parameters for three important compounds, specifically Na_3Sb , NaK_2Sb , and Na_2KSb , as well as their elemental phases. A comparative study will validate the correctness of the computational predictions by comparing them with the optimized results and experimental values.
- The third objective entails investigating the electrical and optical characteristics of mono- and bi-alkali antimonides. This involves examining their band structure, density of states (DOS), dielectric constants, and core spectroscopy. The primary objective is to gain a more profound understanding of the behavior of these compounds in photoemission and photoabsorption applications. The analysis will focus on the specific influence of spin-orbit coupling (SOC) on the electronic structure. Furthermore, the assessment will determine the importance of SOC to various exchange-correlation approximations, including PBE, SCAN, and HSE06.

Chapter 2

Theoretical Framework

2.1 The Many-body Problem in Quantum Mechanics

Acknowledgment that the system consists of electrons and nuclei organized in a distinct electronic configuration at the atomic scale is essential to comprehending our system's many material qualities. This arrangement ultimately determined the physical properties of the solid. The physical properties of the solid are ultimately determined by this arrangement. To examine the actions of quantum particles, we analyze the many-body Schrödinger equation⁷.

$$\hat{H}\Psi = [\hat{T} + \hat{V}]\Psi = \hat{E}_{tot}\Psi \quad (2.1)$$

The symbol \hat{H} represents the Hamiltonian of the system, which includes the operators for kinetic energy (\hat{T}) and potential energy (\hat{V}). The operator \hat{E}_{tot} represents the overall energy of a system and is associated with a many-body wave function. The wavefunction of a system with M nuclei positioned at R_1, R_2, \dots, R_M and N electrons situated at r_1, r_2, \dots, r_N can be expressed as:

$$\Psi = \Psi(r_1, r_2, \dots, r_N; R_1, R_2, \dots, R_M), \quad (2.2)$$

The operator representing kinetic energy (\hat{T}) can be defined as:

$$\hat{T} = -\sum_{i=1}^N \frac{\hbar^2}{2m_e} \nabla_i^2 - \sum_{I=1}^M \frac{\hbar^2}{2M_I} \nabla_I^2, \quad (2.3)$$

In this particular situation, M_I represents the masses of the nuclei, m_e signifies the mass of the electron, \hbar denotes the reduced Planck's constant, and ∇_i^2 and ∇_I^2 are the Laplacian operators that act on the coordinates of electrons and nuclei, respectively. The potential energy operator (\hat{V}) involves three Coulombic interactions that need to be taken into account: electron-electron (\hat{V}_{e-e}), nuclei-nuclei (\hat{V}_{n-n}), and nuclei-electron (\hat{V}_{n-e}).

$$\hat{V} = \hat{V}_{e-e} + \hat{V}_{n-n} + \hat{V}_{n-e} \quad (2.4)$$

At first, we experience the \hat{V}_{e-e} Coulombic repulsion, which is caused by the negative charge of the electrons. This repulsion can be described by the following equation:

$$\hat{V}_{e-e} = \frac{1}{2} \sum_{i \neq j} \frac{e^2}{4\pi\epsilon_0} \frac{1}{|\mathbf{r}_i - \mathbf{r}_j|}, \quad (2.5)$$

The equation employs the symbols e to represent the electron's charge and ϵ_0 to represent the permeability in free space. The indices i and j are defined within the inclusive range of $[1, N]$ and always differ due to the absence of self-repulsion in electrons. The component $\frac{1}{2}$ is included to account for only one energy contribution per electron pair. The positive value of \hat{V}_{e-e} arises from its inherent repulsive characteristic. Furthermore, we experience the \hat{V}_{n-n} Coulombic repulsion, which is expressed by the subsequent equation:

$$\hat{V}_{n-n} = \frac{1}{2} \sum_{I \neq J} \frac{e^2}{4\pi\epsilon_0} \frac{Z_I Z_J}{|\mathbf{R}_I - \mathbf{R}_J|}, \quad (2.6)$$

Here, $Z_{I(J)}$ represents the atomic numbers of each element. Our analysis necessitates the consideration of three factors. The equation (2.5) and its indexing logic and contributions are also applicable to equation (2.6). Furthermore, we encounter the \hat{V}_{e-n} Coulombic repulsion, which emerges due to the negative charge properties of electrons and nuclei. The \hat{V}_{n-e} Coulombic attraction results from the opposing charges of electrons and nuclei. The equation that defines it is as follows:

$$\hat{V}_{n-e} = - \sum_{i,I} \frac{e^2}{4\pi\epsilon_0} \frac{Z_I}{|\mathbf{r}_i - \mathbf{R}_I|}, \quad (2.7)$$

The indexing methodology employed in equations (2.5) and (2.6) can likewise be extended to equation (2.7). This contribution is beneficial due to its appealing characteristics. By replacing the equations mentioned above with the definitions provided in equation (2.1), we can represent the many-body Schrödinger equation as:

$$\left[- \sum_{i=1} \frac{\hbar^2}{2m_e} \nabla_i^2 - \sum_{I=1} \frac{\hbar^2}{2M_I} \nabla_I^2 + \frac{1}{2} \sum_{i \neq j} \frac{e^2}{4\pi\epsilon_0} \frac{1}{|\mathbf{r}_i - \mathbf{r}_j|} + \dots \right. \\ \left. + \frac{1}{2} \sum_{I \neq J} \frac{e^2}{4\pi\epsilon_0} \frac{Z_I Z_J}{|\mathbf{R}_I - \mathbf{R}_J|} - \sum_{i,I} \frac{e^2}{4\pi\epsilon_0} \frac{Z_I}{|\mathbf{r}_i - \mathbf{R}_I|} \right] \Psi = E_{tot} \Psi, \quad (2.8)$$

It is crucial to emphasize that the wavefunction corresponding to a particular set of coordinates (2.2) cannot be directly measured in experiments since it does not reflect a physical quantity that can be observed⁸. Conversely, the physically significant measured quantity is the probability of encountering N electrons at places r_i .

$$|\Psi|^2 = |\Psi(\mathbf{r}_1, \dots, \mathbf{r}_N; \mathbf{R}_1, \dots, \mathbf{R}_M)|^2 \quad (2.9)$$

Subsequently, the probability of locating any electron (regardless of the i label) at position r is determined by⁹:

$$n(r) = N \int |\psi|^2 dr_2 \dots dr_N dR_1 \dots dR_M \quad (2.10)$$

Normalizing the wavefunction (2.2) to 1, we obtain:

$$\int |\Psi|^2 dr_2 \dots dr_N dR_1 \dots dR_M = 1$$

Integrating the electronic charge density over the entire volume equals the total number of electrons when the constraint of the equation is introduced into (2.10).^{8,9}

$$\int n(r) dr = N \quad (2.12)$$

It should be emphasized that using analytical methods to solve the equation (2.8) for systems larger than a Helium atom is exceedingly challenging. Numerical solutions require significant computational resources. This is because the solution's complexity increases exponentially as the number of atoms in the system increases. We can simplify equation (2.8) by employing atomic units⁹ to streamline computations. Thus, it is independent of any empirical parameter. Hence, it is a methodology that analyzes material attributes from fundamental principles. By employing the procedure described in the reference⁹, we can rewrite the equation (2.8) using the Hartree unit, resulting in a more concise expression. The given expression of the many-body Schrodinger equation is widely used in material modeling based on fundamental principles. This many-body Schrödinger equation shows that there are just two needed parameters to complete the equation depending on the material to be analyzed: the atomic numbers (Z_I) and the atomic masses (M_I).

$$\left[-\sum_{i=1}^N \frac{1}{2} \nabla_i^2 - \sum_{I=1}^M \frac{1}{2} \frac{\nabla_I^2}{M_I} + \frac{1}{2} \sum_{i \neq j} \frac{1}{|\mathbf{r}_i - \mathbf{r}_j|} + \frac{1}{2} \sum_{I \neq J} \frac{Z_I Z_J}{|\mathbf{R}_I - \mathbf{R}_J|} - \sum_{i,I} \frac{Z_I}{|\mathbf{r}_i - \mathbf{R}_I|} \right] \Psi = E_{tot} \Psi \quad (2.13)$$

2.1.1 Density Functional Theory (DFT) principles

2.1.1.1 The Hohenberg-Kohn Theorem

Using the independent electron approximation enabled us to streamline the depiction of the many-electron system by including the product of single-particle wavefunctions instead of the whole wavefunction¹⁰. This section will explore advanced concepts beyond the study of the Hohenberg-Kohn and Kohn-Sham methods, which offer more comprehensive approaches to the many-body issue. Typically, the computational calculations for the energy of a quantum state are difficult since the energy E_0 depends on the full wavefunction $\Psi(r_1, r_2, \dots, r_N)$. To determine the value of E_0 , solving a system of $3N$ variables is necessary. Hohenberg and Kohn devised an alternate theory wherein the calculation of E_0 is contingent upon the electron density $n(r)$, which is determined by only three factors¹¹. This statement pertains to the Hohenberg-Kohn theorem, which states that the ground state energy E is a functional of the electron density $n(r)$ (equation 2.14), and the excited state energy E is a functional of the entire many-body wavefunction Ψ (equation 2.15)¹².

$$E = F[n(r)] \quad (2.14)$$

$$E = F[\psi(r_1, r_2, \dots, r_N)] \quad (2.15)$$

The following argument illustrates a fundamental correlation in quantum physics through three essential claims. The energy of the ground-state electron has a direct and exclusive influence on the external potential of the nuclei⁸. Furthermore, the many-body wave function is exclusively dictated by this external potential. The many-body wave function determines the system's total energy. The logical sequence highlights the interconnectedness of these aspects and is substantiated by the induction process. The demonstration relies on the fundamental premise that the ground state energy represents the minimum attainable energy of the system, whereas all other states exhibit higher energy levels^{9,11}. It has been demonstrated that two distinct external potentials can yield the same ground-state energy. This counterintuitive claim highlights the strength and resilience of the proof's logical framework. The derivative of the functional evaluated at the ground state density, which minimizes the total energy, is determined by the ground state density¹².

$$\left. \frac{\delta F[n]}{\delta n} \right|_{n_0} = 0 \quad (2.16)$$

2.1.1.2 The Kohn-Sham equation

We examined the Hohenberg-Kohn theorems in the preceding part, which offered no valuable guidance on constructing the functional⁷. To address this issue, Kohn and Sham put up a resolution by incorporating an exchange and correlation term to account for interactions beyond the assumption of independent electrons. At first, the kinetic and Coulomb energies were designated as operators. The first term directly depends on $n(r)$, whereas the kinetic and Coulomb terms indirectly depend on it. Kohn and Sham proposed enlarging these terms and incorporating an extra exchange-correlation term to tackle the discrepancies¹³.

$$\hat{T} = - \sum_1 \frac{1}{2} \nabla_i^2, \quad (2.17)$$

$$\hat{W} = \frac{1}{2} \sum_{i \neq j} \frac{1}{|r_i - r_j|}, \quad (2.18)$$

Then, the energy becomes:

$$E = F[n] = \int dr n(r) V_n(r) + \langle \psi[n] | \hat{T} + \hat{W} | \psi[n] \rangle \quad (2.19)$$

The kinetic and Coulomb terms are implicit, whereas the first term is explicitly dependent on $n(r)$. Kohn and Sham suggested augmenting these terms by incorporating an additional exchange-correlation term to accommodate the disparity:

$$E = F[n] = \int d\mathbf{r} n(\mathbf{r}) V_n(\mathbf{r}) - \sum_i \int d\mathbf{r} \phi_i^*(\mathbf{r}) \frac{\nabla^2}{2} \phi_i(\mathbf{r}) + \frac{1}{2} \int \int d\mathbf{r} d\mathbf{r}' \frac{n(\mathbf{r})n(\mathbf{r}')}{|\mathbf{r} - \mathbf{r}'|} + E_{xc}[n], \quad (2.20)$$

In the context of the independent electron approximation, we only consider the terms that do not involve the exchange-correlation energy, denoted as E_{xc} . The E_{xc} energy encompasses all the omitted components. By establishing the value of E_{xc} , it becomes feasible to compute the energy of the ground state by utilizing the electron density, $n(r)$. The Hohenberg-Kohn variational principle, we may get the electron density, denoted as n_0 , which minimizes the total energy functional $F[n]$, as seen in equation (2.16)⁸. Consequently, we may construct the subsequent limitation for the orbitals:

$$\frac{\delta F}{\delta \phi_i^*} = 0 \quad (2.21)$$

Applying this constrain we obtain a similar problem than in Hartree-Fock theory which can be approached using the Lagrange multipliers technique if the functional

$E = F[n]$ is included. In addition, we may utilize the HK variational method to deduce the individual wave functions $\phi_i(r)$ and form the electron density n . Consequently, we arrive at the subsequent outcome:

$$\left[-\frac{\nabla^2}{2} + \hat{W}_{en}(\mathbf{r}) + \hat{W}_H(\mathbf{r}) \right] \phi_i(\mathbf{r}) + \int d\mathbf{r}' V_{xc}(\mathbf{r}, \mathbf{r}') \phi_i(\mathbf{r}') = \epsilon_i \phi_i(\mathbf{r}), \quad (2.22)$$

When all terms in the Hartree-Fock equations are indistinguishable, the exchange-correlation potential $V_{xc}(r)$ can be introduced as an additional term. The system of equations shown in (2.22) is the Kohn-Sham equations and is the foundation of the Kohn-Sham theory.

$$V_{xc}(\mathbf{r}) = \left. \frac{\delta E_{xc}[n]}{\delta n} \right|_{n(\mathbf{r})} \quad (2.23)$$

In essence, Kohn-Sham's theory elucidates a theoretical scenario in which electrons engage in mutual interactions via an external potential. The theory delineates the principal interaction effects among the electrons while simplifying the unknown contributions to the exchange and correlation energy E_{xc} and potential V_{xc} . The accuracy of DFT computations relies heavily on the precise creation of the exchange-correlation energy denoted as E_{xc} ¹¹.

2.1.2 Exchange-correlation functional E_{xc}

Materials modeling has extensively investigated Density Functional Theory (DFT). Many techniques have been devised to address practical issues and attain precise estimations. The Kohn-Sham theory and DFT (KS-DFT) are successful and extensively employed theories in material science. Nevertheless, the essential component of KS theory, the exchange-correlation energy factor E_{xc} , has yet to be included¹². The exchange functional E_x and the correlation functional E_c express it (Eq. 2.24), where ϵ_x and ϵ_c represent the energy per particle¹⁴. Various approximation approaches have been devised to achieve high accuracy in fitting a functional to any given material environment. These methods can be categorized as either non-empirical, satisfying additional constraints, or semi-empirical, augmenting unknown coefficients¹³. Unlike the many-body wave function, the DFT method does not possess the property of systematic improvement. Integrating additional contributions into the model to adhere to more precise constraints does not ensure enhancement in all pertinent interactions.

$$E_{xc}[\rho] = E_x[\rho] + E_c[\rho] = \int \rho(r)\epsilon_x[\rho(r)]dr + \int \rho(r)\epsilon_c[\rho(r)]dr \quad (2.24)$$

This part will explore the challenges associated with employing approximation functionals. The issues encompass managing diverse interactions, addressing self-interaction faults, and ensuring numerical precision. As we aim for greater precision, the computing expense rises, which can be depicted by the many levels on Jacob's ladder of complexity. The following part will examine three often employed functionals: PBE, SCAN, and HSE06.

2.1.2.1 The Local Spin Density Approximation (LSDA)

Within the realm of DFT John Perdew introduced a hierarchical system called Jacob's Ladder to categorize the various degrees of approximation¹⁵. The hierarchy is established according to the Hartree theory, assuming a zero exchange-correlation energy and a fully classical electron interaction.

The Local Spin Density estimate (LSDA) is Jacob's Ladder's lowest rung and the most basic estimate for exchange-correlation energy¹². This approximation assumes that the material may be modeled as an electron gas with a consistent and even density distribution. The LSDA approximation solely relies on the local spin densities n_\uparrow and n_\downarrow for the determination of the exchange-correlation energy E_{xc} .

$$E_{xc}^{LSDA}[n_\uparrow, n_\downarrow] = \int d^3r e_{xc}^{ho}(n_\uparrow(\mathbf{r}), n_\downarrow(\mathbf{r})) \quad (2.25)$$

The LSDA approach is highly precise in its ability to forecast the characteristics of a homogeneous electron gas. However, it cannot accurately forecast the characteristics of other tangible systems, such as small groups of atoms and molecules¹⁶. Although it remains commonly employed for predicting the characteristics of solids due to its precision, it produces excessively elevated outcomes for the atomization energies of molecules. LSDA is not very effective in forecasting the characteristics of atoms and molecules due to their limited similarity to a homogeneous electron gas¹⁷. This method was created to deal with a uniform electron gas. In this case, LSDA underestimates the exchange energy by about 10%. This leads to larger errors. Additionally, electron correlation is usually overestimated by approximately 100 kJ/mol. As a result, the method generates results similar to those obtained using Hartree-Fock methods¹⁴.

2.1.2.2 The generalized gradient approximation (GGA)

The generalized gradient approximation (GGA) uses an improved local spin density approximation (LSDA) version to determine the exchange-correlation energy. The GGA functional has gained significant popularity in solid-state physics and quantum chemistry throughout the years^{13,15,17,18}. This functional incorporates additional terms expressed in the spin densities' gradients; Kohn and Sham proposed an approximation for the exchange-correlation potential in their fundamental research derived from the second-order gradient expansion (GEA), which applies only to densities that vary slowly. GGAs incorporated supplementary local density gradients to address the non-uniform density distribution encountered in LSDA^{19,20}. Here, the first derivative of the density is included as a variable, and it is derivated at a given point, differentiating from Hartree-Fock exchange energy, which uses a space volume to derivate²⁰.

GGA functionals have shown an exceptional ability to achieve chemical precision, with errors as low as $0.1eV$, across various chemical processes. Notwithstanding their potential, GGA approximations demonstrate specific constraints²⁰. Significantly, they offer an insufficient depiction of van der Waals forces, which play a vital role in numerous molecular interactions. In addition, GGA and LDA tend to underestimate the magnitude of band gaps, leading to prediction disparities²¹. A further obstacle arises from the imprecise forecasting of magnetization in systems with significant correlations.

2.1.2.3 The PBE functional

In their fundamental research, Kohn and Sham proposed an approximation for the exchange-correlation potential, represented as v_{xc} . This approach applies the same treatment to exchange and correlation effects as to the homogeneous electron gas, which means that the density is a function varying slowly. The Generalized Gradient Approximation (GGA) is a more precise estimation method for v_{xc} , considering both the local electron density and its gradient. In this study, we employ the PBE (Perdew-Burke-Ernzerhof) parameterization of GGA, which is renowned for its remarkable precision in forecasting the structural properties of materials. The utilization of PBE in materials research is extensive due to its effective representation of bond lengths, angles, and other structural characteristics.

While PBE is highly proficient in producing predictions about the structure of materials, its accuracy in predicting electrical properties may be somewhat limited. Specifically, the PBE method tends to underestimate the magnitude of band gaps and may encounter challenges in accurately depicting electronic phenomena. Hence, it is recommended to use prudence when employing PBE for investigations that rely significantly on precise electronic property predictions²².

2.1.2.4 The SCAN functional

The non-empirical SCAN meta-GGA, a novel density-functional theory, was introduced in 2015. This marked a substantial progression in this domain. The functional was formulated by Jianwei Sun, Adrienn Ruzsinszky, and John P. Perdew, together with the PBE (GGA) functional co-creators. SCAN complies with all 17 established precise conditions for a meta-GGA, rendering it a cutting-edge functional. The initial meta-GGA fulfills complete constraint satisfaction^{23,24}.

The equation SCAN uses is a non-linear integral equation describing the total energy of an electronic system. It can be written as:

$$E = \int \rho(\mathbf{r})v_S(\mathbf{r})d\mathbf{r} + \frac{1}{2} \int \int \frac{\rho(\mathbf{r}_1)\rho(\mathbf{r}_2)}{r_{12}}d\mathbf{r}_1d\mathbf{r}_2 + E_{XC}[\rho] \quad (2.26)$$

where $\rho(r)$ is the electron density $v_S(r)$ is the electrostatic potential and $E_{XC}[\rho]$ is the exchange correlation energy. This equation is solved iteratively, using methods like finite differences or finite elements¹⁷.

Furthermore, the definition of the exchange-correlation energy can be expressed as:

$$E_{XC}^{SCAN}[\rho] = \frac{1}{2} \int \int \frac{\rho(\mathbf{r}_1)\rho(\mathbf{r}_2)}{r_{12}}f(\mathbf{r}_1, \mathbf{r}_2)d\mathbf{r}_1d\mathbf{r}_2 \quad (2.27)$$

where $f(r_1, r_2)$ is a function of the electron density and the distance between two points. This function is chosen to make SCAN fulfill certain conditions like exchange symmetry, rotational invariance, and translational invariance¹⁷. The SCAN approach utilizes the parameter α to accurately forecast geometries and energy for several types of bonds, such as covalent, metallic, ionic, hydrogen, and van der Waals bonds. It exhibits superior performance compared to GGAs. Subsequent research has demonstrated that SCAN can achieve or exceed the precision of computationally intensive hybrid functionals while maintaining a comparable cost to GGAs⁷. The efficacy of SCAN relies on 17 limitations, including tight lower bound, rare-gas atoms, and nonbonded interaction.

Furthermore, SCAN considers several suitable standards, including consistent and gradually changing densities, jellium surface energy, the hydrogen atom, the helium atom, and thresholds for rare-gas atoms²⁵. SCAN excels in accurately forecasting van der Waals interactions within the intermediate range. It offers distinct advantages over the PBE functional in various circumstances, including the characterization of semiconductor defects and specific metal oxides⁸.

2.1.2.5 The HSE06 functional

HSE06 is a highly effective hybrid functional that combines Hartree-Fock exchange with well-known DFT functionals such as PBE. The distinctive combination of elements in HSE06 enables it to produce notably enhanced outcomes, particularly for semiconductors and insulators. HSE06 offers a promising solution for reliably anticipating band gaps²⁶. The predictions of this method exceed those of conventional DFT functionals, providing researchers with a more precise understanding of the energy needed to elevate an electron from its lowest energy state to a higher level. The knowledge provided is essential for developing novel materials with customized electronic characteristics, facilitating progress in several domains such as photovoltaics and optoelectronics²⁷. However, HSE06 does not end at that point. Its expertise goes beyond the range of energy levels that electrons cannot occupy, extending into the fascinating realm of electrons in higher energy states²⁸. In contrast to normal DFT functionals, its calculations exhibit higher computational demands, necessitating increased resources and time.

2.2 Ultra-bright Electron Beams

Scientific advances in materials innovation are driving the progress of current technology. Many technologies operate based on electron sources, ranging from daily appliances like televisions and X-ray machines to medicine and complex systems like particle accelerators²⁹. Due to their versatility and applicability in both theoretical and applied fields, extensive research has been conducted to develop better electron sources with high efficiency, long operation life, and low thermal emittance³⁰.

The principle of operation for electron sources is based on generating an electron beam through a photocathode. These cathodes require an energy source to accelerate, which can be thermal, electric, or photon-based. Electric fields are the most commonly used due to their advantages over other methods²⁹. An electric field is a region of space where electrically charged particles experience a force. The force

on an electron in an electric field is proportional to its charge and the strength of the field. The force acts away from the positive electrode and towards the negative electrode, giving the electrons the energy necessary to reach high speeds³¹. As the electrons move through the electric field, they gain energy, the amount of which depends on the strength of the field and the distance traveled. The effect of magnets causes the electrons to travel in a straight line, thereby focusing them into a small, concentrated beam of particles, creating a high-energy beam of electrons³². A vacuum environment protects the process from residual problems such as electron scattering on gas molecules, residual particles, and photocathode contamination. The electric field applied can differ into three injector types, depending on its nature: Direct Current (DC), Radio Frequency (RF), and Superconductivity Radio Frequency (SRF). Our interest lies in RF injectors with a cathode surrounded by a specially shaped resonance in the cavity, eliminating the need for an anode. Such RF electron sources are used in Deutsches Synchrotron (DESY), the European Organization for Nuclear Research (CERN), and the Paul-Scheerer Institute (PSI)³³.

2.3 Photocathode Materials

As mentioned, cathodes serve as the source of the generated electrons, and they can be made of either a metal or a semiconductor material. The selection of suitable cathodes depends on several factors, such as high Quantum Efficiency (QE) at the convenient laser wavelength, long lifetime, fast response time, and low thermal emittance³⁴. Semiconductor photocathodes like cesium telluride (Cs_2Te), alkali and bi-alkali antimonides (K_2CsSb), or gallium arsenide (GaAs) are commonly used to meet the requirement of higher bunch charges and corrections.

The maximum brightness per photoelectron (B_{max}) is determined by two factors: the electric field on the surface of the photocathode material that generates the electrons and the momentum spread of the photoemitted electrons along the surface of the cathode³⁵.

$$B_{max} \approx \frac{E_{norm}}{MTE} \quad (2.28)$$

The E_{norm} symbol represents the electric field's component along the photocathode's surface normal. The mean transverse energy (MTE) measures the momentum spread and shows the photoelectron's normal kinetic energy along the surface of the photocathode. Therefore, it is essential to reduce the MTE (around 10 meV)^{36,37}, which depends on the composition and surface properties of the photocathode³⁸,

to optimize the maximum value of B_{max} regardless of the type of instrument. Surfaces that are extremely smooth at an atomic level help reduce the undesired rise in MTE (mean time between failures) caused by physical roughness and chemical inconsistencies³⁹. Additionally, materials made up of a single crystal have clearly defined electronic structures that may be utilized to produce photoelectron beams with low MTEs⁶. Semiconductors produce more concentrated electron beams due to their greater quantum efficiencies, which refers to the ratio of photoemitted electrons to incident photons. This characteristic is crucial for various high-current applications^{6,38}.

Electron-phonon scattering is a significant phenomenon in semiconductors that can lead to considerable changes in the momentum of electrons. This, in turn, can significantly impact the Mean Time to Escape (MTE) of the resulting photoelectron beam. Therefore, to gain a basic understanding of the factors that influence the electronic and optical behavior of a photoelectron beam and to predict the maximum potential of a semiconducting photocathode material, it is essential to conduct an *ab initio* investigation of photoemission processes in crystal semiconducting photocathode materials. This investigation is the central focus of this thesis.

2.3.1 Mono- and bi-alkali antimonides

Better electron emitters can be made using mono- and bi-alkali antimonides, or X_2YSb compounds, where X and Y are elements from Group I of the periodic table. These compounds can generate electron beams of exceptional purity. Nevertheless, understanding these materials is still limited, mostly because of the technical difficulties in growing pure and well-organized alkali antimonides. There is insufficient comprehension of these materials' mechanically stable crystal structures in the existing literature^{2,40-42}. Furthermore, after successful growth, single-crystal forms of these materials are highly susceptible to vacuum conditions. They can only survive in ultra-high vacuums when they are in their thin film states. This poses significant challenges for experimental investigations into their structural and optoelectronic properties⁴¹.

In recent years, there has been a notable rise in the usage of semiconductor materials for different purposes. Among these materials, alkali antimonides have gained popularity due to their remarkable properties^{43,44}. Photocathodes made of Cesium telluride (Cs_2Te) are widely used in the semiconductor industry for accelerator applications. These photocathodes are known for their durability in high-gradient environments and ability to convert ultraviolet (UV) light into electrical

current. However, the laser systems used with these photocathodes pose challenges as they require complex setups and high-intensity infrared (IR) laser light⁴⁵. These factors contribute to higher operational expenses and lower conversion efficiency across multiple stages. A couple of alternatives to Cs₂Te are worth considering. One option is gallium arsenide (GaAs), which has a high quantum efficiency (QE) of approximately 10% in the visible spectrum. However, GaAs have a longer response time of tens of picoseconds and are quite sensitive to radio frequency (RF) interference^{46,47}. Another possibility is alkali antimonide photocathodes, specifically cesium-potassium-antimonide, which have a relatively high QE of around 10% in the green wavelength range. These photocathodes offer a quick response time and low thermal emittance, making them a strong contender for applications requiring a highly bright beam of light. Still, alkali antimonide compounds need a better vacuum (10–11 mbar) than Cs₂Te (10–10 mbar) to keep their quantum efficiency high^{48,49}.

The quantum efficiency (QE) and thermal emittance parameters have shown highly encouraging results using these photocathodes. However, to further increase the intensity of the electron beam in future continuous wave (CW) guns, achieving even higher cathode gradients (30-40 MV/m) for various purposes⁵⁰. Our ongoing research centers on developing multi-alkali photocathode materials (Na-K-Sb) and studying their electronic and optical properties using *ab initio* methods. Despite differences in crystal structures and notable imperfections, modern density functional theory, based on the first principles technique, can reliably predict a material's optical, electrical, and magnetic properties.

Photocathode Material	Advantages	Disadvantages
Metals (Cu, Mg, Pb)	Durable and responsive, withstand years of use with less than a picosecond response time.	Easier to prepare than semiconductors, high work function, requiring UV light.
Cesium Telluride	The preparation process ensures quantum efficiency values between 10 and 20% under UV excitation while maintaining a reasonable lifetime, fast response time, and survivability under RF fields.	Intense UV light is required, making it vulnerable to vacuum instabilities, especially O ₂ and CO ₂ . However, reviving the contaminated cathode with UV light and extra heat treatment is possible.
Alkali-metal antimonide	This photocathode has a quantum efficiency (QE) of 4-12% at 532 nm and low thermal emittance. Its main advantage is its spectral response under green light, which is why it's also known as the "green cathode." This type of cathode is more efficient than other materials that operate under UV light, as it only requires the second harmonic transformation of the laser, thus relieving the laser system.	Preparing for optimal composition to maximize quantum efficiency (QE) and longevity can be a complex task with its own challenges. Remembering the limited lifetime of RF fields and the potential risk of cavity contamination in (S)RF injectors is important.

TABLE 2.1: Comparison of photocathode materials generally used in photoemission applications²⁹.

Photocathode Material	Advantages	Disadvantages
Gallium Arsenide	This material is readily available for commercial purposes and has reproducible quality. The supplier guarantees the desired quality and dopant concentrations. It exhibits an excellent spectral response to near-infrared (NIR) and low dark current, making it an ideal choice for vacuum photodetectors. One of the added advantages of this material is that it does not require UV light to generate spin-polarized electrons.	Cs and O ₂ are used in an intricate process to activate. Additionally, maintaining stable ultra-high vacuum (UHV) conditions is crucial. The photocathode has a limited lifetime and is susceptible to multi-packing and associated risks when exposed to a radio frequency (RF) field.
Gallium Nitride	Although <i>p</i> -GaN requires UV light, similar to other photocathodes, its spectral response can be modified by adjusting the E_{gap} with specific dopant atoms. Moreover, preparing <i>p</i> -GaN is simpler than other semiconductor cathodes, and activation can be simplified by using only Cs. Another advantage is restoring this cathode using a thermal treatment to remove surface pollutants after degradation.	Some parameters require further investigation, as information on thermal emittance and response time is incomplete or outdated.

TABLE 2.2: Continued from Part 1²⁹.

Chapter 3

Methodology

3.1 Computational Details

The computational aspects of the study were conducted using the FHI-aims code developed by the Fritz Haber Institute. This widely respected software tool is tailored to ab initio calculations based on quantum-mechanical first principles. The calculations were performed on the High-Performance Computing Center infrastructure at the University of Oldenburg. They involved multiple stages, systematically accounting for spin-orbit coupling effects and incorporating diverse functionals. The FHI-aims program is a powerful tool for describing the behavior of electrons in molecules. It uses different self-energy formalisms and wave-function-based molecular total energy calculations based on Hartree-Fock and many-body perturbation theory⁵¹. The program works as an all-electron electronic structure code and uses localized, numerically tabulated atom-centered basis functions to discretize orbitals and wave functions within electronic structure theory. This approach ensures a highly precise representation of orbitals and density for complex nanostructures across the periodic table, covering all core and valence electrons without relying on shape approximations in potentials or wave functions⁵².

The program uses a basis set called Numeric Atom-Centered Orbital (NAO)⁵³. This feature allows creating element-specific basis sets that balance compactness and high transferable accuracy, achieving total energy convergence at the millielectronvolt level in production calculations. This implementation proves the effectiveness of the algorithms, achieving accurate all-electron, full-potential computational quantum mechanics with efficiency comparable to the fastest plane-wave pseudopotential schemes. Moreover, the approach can handle systems with thousands of atoms and scale efficiently on various hardware, from individual PCs to massively parallel computers with thousands of CPUs⁵⁴.

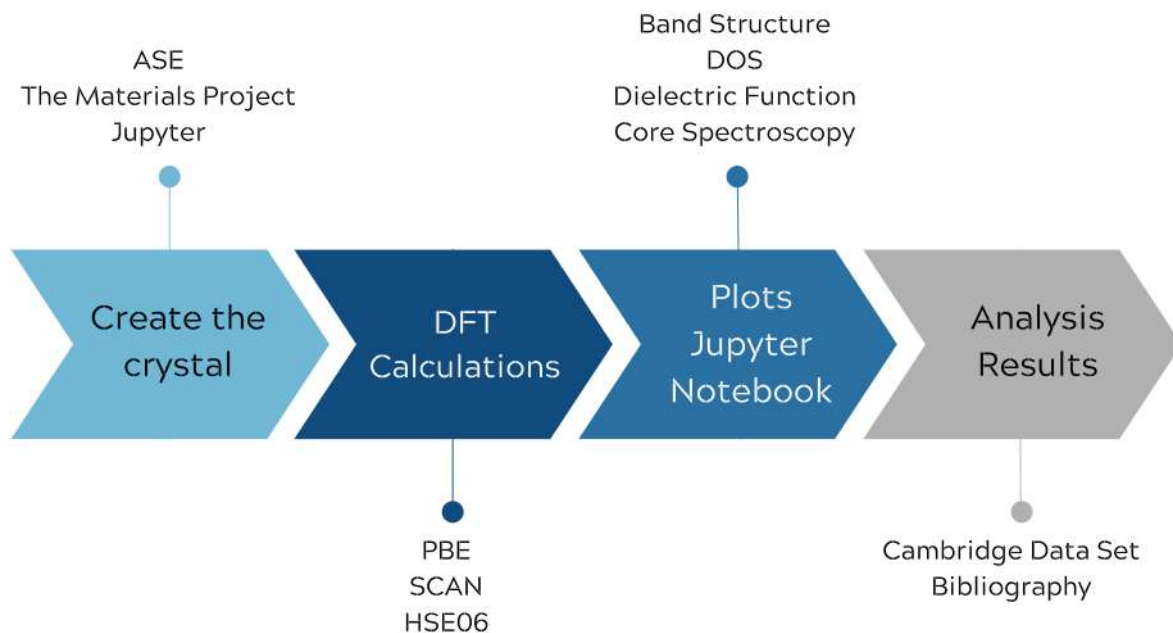


FIGURE 3.1: Workflow developed in the present work.

FHI-aims requires two separate input files, `control.in` and `geometry.in`, located in the directory where the FHI-aims binary is initiated.

The `geometry.in` file specifically contains information about the atomic structure for a given calculation. This includes atomic positions and details about each element or species specified in `control.in`. Additionally, lattice vectors can be defined if the calculation involves periodicity. Any other relevant information is included here only if it directly relates to the respective atom, such as initial charge, initial spin moment, or relaxation constraints. The order of lines is not important, except that data specific to a particular atom must follow the line designating that atom and come before any subsequent atom specifications⁵¹.

On the other hand, `control.in` consolidates all other runtime-specific details. Typically, this file includes a general section where the order of lines is not significant. Additionally, the file includes species subtags referenced by `geometry.in`. The line order is once again unimportant within the description of a given species. Still, all details related to the same species must follow the initial species tag in a cohesive block⁵¹. In both files, the units of measurement are specified as Ångströms for length parameters and electron volts (eV) for energies; derived quantities are adjusted accordingly.

Material	International Number	Space Group	Lattice System
Na	194	$P6_3/mmc$	Hexagonal
Sb	166	$R\bar{3}m$	Rhombohedral
K	229	$Im\bar{3}m$	Cubic
Na ₃ Sb	194	$P6_3/mmc$	Hexagonal
NaK ₂ Sb	186	$P6_3/mmc$	Hexagonal
Na ₂ KSb	225	$Fm\bar{3}m$	Cubic

TABLE 3.1: Data used for the generation of inputs used in Jupyter.

3.2 Workflow

Several steps were undertaken to better understand the electronic and optical properties of the materials under consideration. These steps included the creation of inputs from scratch. A Jupyter Notebook was used to define the geometric properties of each crystal. The Atomic Simulation Environment (ASE) package was employed to assist in this task^{55,56}, and SeeK-path, a module to obtain band paths in the Brillouin zone of crystal structures^{57,58}, here the bravais lattice is detected properly using the spacegroup symmetry. Each crystal was given a unique identifier based primarily on its crystallographic information, which can be found in Table 3.1. Initially, the code uses the ASE package to obtain the crystal's atomic positions and cell parameters after providing it with the inputs above.

To graph the electronic eigenstates, it is typical to trace a path within the 1st Brillouin zone of the crystal, covering all the significant high-symmetry points. The SeeK-path library can identify the symmetry of the crystal and provide a suggested path. This involves creating a primitive structure with a specific orientation and path parameters specific to that structure and identifying the high symmetry points. We can create the input file for FHI-aims with all this information.

The computational techniques used in this study, including spin-orbit coupling, FHI-aims, and different density functionals, enabled a thorough examination of the electrical and optical characteristics of several sodium antimonide phases. These calculations are a solid basis for additional experimental research and offer insightful information for creating cutting-edge materials for vacuum electron sources in particle accelerators.

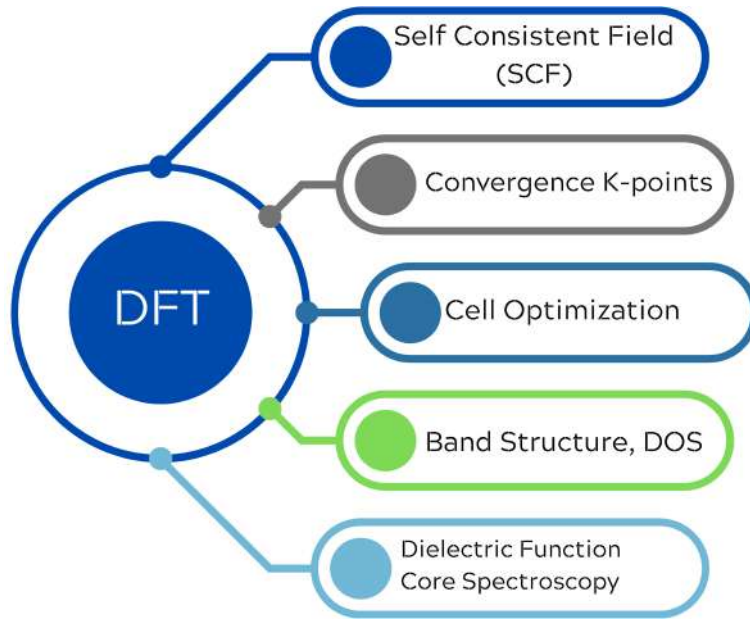


FIGURE 3.2: DFT workflow applied in order to elucidate the electronic and optical properties of the materials proposed in the present work.

3.2.1 Self Consistent Field Calculations

The Kohn-Sham (KS) equations determine the ground state's energy and electron density. To achieve self-consistency in these equations, the solutions of the electronic states (ϕ_i) must coincide throughout the iterative process. The process begins by calculating the nuclear potential by specifying the nuclear coordinates. Then, an approximation is made for V_H and V_{xc} by guessing the electron density based on isolated atomic positions.

This is used to solve for V_{tot} , which produces new wavefunctions to estimate the electron density. The iterative procedure continues until it converges to a desired tolerance concerning the initial assumption, which indicates self-consistency. It starts with calculating the nuclear potential, followed by guessing an initial electron density based on isolated atoms arranged in materials position to determine V_H and V_{xc} , and consequently V_{tot} . This way, the numerical solution produces a new wave function to estimate the density. The iterative process ends when the newly estimated density matches the initial one under a desired tolerance.

3.2.2 Convergency k-points and Cell Optimization

K-point sampling is crucial in determining a system's unit cell's electron density based on size and symmetry⁵². Accurately selecting these sampling points is essential for reliably calculating electronic and optical properties. The number of points

Material	K-grid			
Na	4x4x2	6x6x3	12x12x7	15x15x8
Sb	4x4x1	8x8x2	18x18x6	26x26x9
K	4x4x4	8x8x8	12x12x12	16x16x16
Na ₃ Sb	4x4x2	8x8x4	12x12x6	16x16x8
NaK ₂ Sb	4x4x2	8x8x4	12x12x5	14x14x6
Na ₂ KSb	4x4x4	8x8x8	12x12x12	14x14x14

TABLE 3.2: Highlighted Grid Convergence: In this table, all checked grids are displayed, with the converged ones emphasized in bold for easy identification.

required depends on the size of the Brillouin Zone, and there are various methods for selecting the appropriate set of k-points⁵⁹. This thesis comprehensively compares four combinations of k-grids to determine the most accurate and efficient k-point combinations for integrating periodic functions of the wave vector. The comparison process involves evaluating the energy outcomes of each combination and highlighting the optimal choices in Table 3.2. The chosen options, determined through careful energy analysis, are presented in bold for easy reference.

Every system must go through a proper relaxation process to ensure accurate and reliable results. This involves precisely adjusting the atomic positions and cell parameters to determine the electronic and optical properties of different crystal and elemental phases⁴. Thorough relaxation is essential for studying materials and comprehensively understanding their properties. The meticulous selection of k-point combinations and proper relaxation procedure is crucial for accurately calculating electronic and optical properties⁶⁰.

3.2.3 Band Structure and Density of States

When exploring a material's electronic structure, the electronic density of states (DOS) is a crucial metric, as it comprehensively describes its electronic properties⁶¹. When analyzing periodic systems, the DOS specifically refers to the density of electronic states per unit of energy and per unit of volume³⁹. In DOS graphs, energy is usually measured relative to the Fermi energy (E_f). This represents the highest occupied electronic state at zero temperature ($T = 0$ K)⁶². One must integrate the electronic density obtained from density functional theory (DFT) calculations across k-space to calculate it. This information is then used to identify the valence and conduction bands. The valence band contains all occupied electronic states, while the conduction band includes all unoccupied states⁶³.

Whether a material is classified as a semiconductor, metal, or insulator depends on the presence or absence of a separation between two bands. This separation is commonly known as the bandgap and contains no electronic states^{64,65}. Additionally, the properties of this bandgap determine the practical applications of semiconductors in various technological fields. The PDOS, which stands for Projected Density of States, shows how a particular orbit of a specific atom contributes to the density of states. If you add all the projections, you will get the total density of states, known as the DOS^{61,66}. The electronic density can be broken down into components linked to specific orbitals to understand localized states within a material better. This is known as the Partial Density of States (PDOS), defined as the number of electronic states with energies weighted by the fraction of the total electron density corresponding to the volume surrounding a nucleus. Calculating band structure and density of states (DOS) provides essential information on the energy dispersion of electrons in a material and the identification of significant electronic states that contribute to its properties⁶⁷.

After examining the structural characteristics and stability of the materials under consideration, we will now focus on their electronic structure, which is necessary to fully comprehend their behavior as photocathode materials. To this end, we will first analyze their band structure and density of states (DOS), which we will further deconstruct into contributions from individual atoms.

3.2.4 Dielectric Function Calculations

The complex dielectric function $\epsilon(\omega)$ (DF) is commonly used to characterize the linear response of a material to an external electric field. For crystals that do not have cubic symmetry, the DF is a tensor of second rank. Based on the groundbreaking research conducted by previous scholars^{68,69}, who utilized the random phase approximation (RPA) to determine the linear response of periodic crystals, the imaginary component of the dielectric tensor $\epsilon_{ij}^{(2)}$ for a system with a gap between occupied and unoccupied states can be expressed as the summation of all interband combinations, with each combination being weighted by the corresponding transition matrix elements⁷⁰

The symbols $|c_k\rangle$ and $|v_k\rangle$ represent the Kohn-Sham orbitals with wave vector k for the conduction and valence bands, respectively. The energies of these bands are denoted by E_{ck} and E_{vk} ⁶⁸. The Cartesian components of the momentum operator are represented by p_j . The variables m , e , ω , and V represent the free electron mass,

electron charges, frequency, and unit cell volume, respectively. The real component $\epsilon_{ij}^{(1)}$ is derived from Eq.3.1 via the Kramers-Kronig transformation. The convergence parameter c , representing the number of empty conduction states included in the sum in Eq.3.1, has been thoroughly verified for all numerical results in this study⁷¹.

$$\epsilon_{ij}^{(2)}(\omega) = \frac{4\pi^2 e^2}{m^2(\omega - \Delta_c/\hbar)^2 V} \sum_{v,c,k} \langle v_k | p_j | c_k \epsilon_{ij}^{(2)} \rangle \langle c_k | p_i | v_k \rangle \times \delta(E_{ck} + \Delta_c - E_{vk} - \hbar\omega) \quad (3.1)$$

Equation 3.1 is obtained using the independent quasi-particle approximation⁷², where the interactions between the excited electron and the remaining hole are ignored. It is assumed that the correction to the Kohn-Sham eigenvalues due to quasi-particles can be represented by a constant correction term Δ_c , independent of the unoccupied conduction states (represented by the scissors operator)⁶⁹. Still, studies of the optical characteristics, such as transmission, reflection, and absorption coefficients, are typically conducted for thin films on a transparent substrate. The ab initio outcome can be utilized to derive these quantities by applying Maxwell's equation for optically anisotropic media and enforcing suitable boundary conditions at the interfaces between neighboring layers. Optically, anisotropic systems require a 4×4 matrix technique to account for multiple reflection and interference effects. This technique extends the conventional 2×2 matrix approach for isotropic layered media^{73,74}.

3.2.5 Core-Level Spectroscopy Calculations

While traditional Core Level Spectroscopy (CLS) relies on experimental techniques like X-ray photoelectron spectroscopy (XPS), advancements in computational power have opened doors to utilizing Density Functional Theory (DFT) as a valuable alternative or complementary approach. This method leverages the power of DFT calculations to simulate the removal of a core electron from a specific atom within a material's crystal structure. This approach offers several advantages, including cost-effectiveness, flexibility in exploring diverse material systems, and access to detailed information beyond binding energies. However, limitations like potential discrepancies with experimental values due to inherent computational challenges (underestimation of 10-20%⁷⁵) necessitate a mindful approach. When strategically combined with experimental data. When we look at the Na-Sb system for photocathode uses, this method can tell us a lot about the core electron binding energies and how these things relate to other electronic properties we get from DFT calculations. The relative core shifts can still provide valuable correlations with X-ray Photoelectron

Spectroscopy (XPS) data. Using an all-electron DFT approach, it becomes possible to access the energies of all core electrons; this allows for a precise and sophisticated investigation of crystals within DFT calculations, particularly when employing core spectroscopy with a delta energy approach to eigenvalues. To know the binding energy of each orbital of the Na and Sb atoms in the different phases, the formula was used:

$$\Delta E = E_b = E_{bulk} - E_{\text{elemental phase}} \quad (3.2)$$

Where ΔE is the energy difference, E_b is the binding energy, E_{bulk} is the eigenvalue of the orbital in the crystalline phase and $E_{\text{elemental phase}}$ is the eigenvalue of the orbital in the corresponding elemental phase. The eigenvalues were obtained from electronic calculations performed in the previous steps. Binding energy is a measure of the stability of the chemical bond between atoms and can vary depending on the phase and geometry of the system. It can be evaluated by comparing the binding energies of the different phases between the Na and Sb atoms.

3.2.6 Spin Orbital Coupling Calculations

In this study, we investigate the effects of spin-orbit coupling on the electronic and optical properties of Na-Sb-based crystals. Spin-orbit coupling is a quantum effect that occurs when a material's motion and the spin of electrons influence each other⁷⁶. This effect is especially important for 4d and 5d transition metals, such as Sb, which have many electrons in their outer shells⁷⁷. Therefore, the spin-orbit coupling can change the energy levels of these materials, depending on their structure and bonding. The spin-orbit coupling strength is measured by the spin-orbit coupling constant (λ_{SO}), which increases with the element's atomic number (Z). The SOC increases from 3d to 5d. For 4d species, the spin-orbit coupling constant ranges from 0.1 to 0.2 eV⁷⁸. Additionally, one can expect a strong influence of SOC in the low-spin state, i.e., very often for 4d and 5d ions, we have only partially occupied t_{2g} levels, so their SOC is indeed instrumental and often crucial⁷⁹.

More calculations were done to determine how SOC affected the three systems we looked at and how well the approximations we used for v_{xc} captured it. The results of this analysis will be compared to the findings discussed earlier.

Chapter 4

Results and Discussion

4.1 Structural Parameters

4.1.1 Cell Optimization

The compound Na_3Sb has a hexagonal crystal structure ($P6_3/mmc$), similar to Na_3As . However, other potential crystal structures exist, such as the cubic structure ($Fm\bar{3}m$), which is less stable thermodynamically. Experimental conditions may also lead to the formation of monoclinic, tetragonal, and orthorhombic phases⁸⁰. The Na_3Sb structure has two equivalent Na^+ sites: Na_1 and Na_2 , as shown in Figure 4.1. Na_1 interacts with six Sb atoms in an octahedral arrangement with a Na-Sb bond distance of 2.74-2.78 Å, while Na_2 has a distorted tetrahedral coordination with four Sb atoms and a larger bond distance of 2.96-3.04 Å. The Na^+ ions in Na_1 sites have higher mobility due to their shorter bonds and lower coordination number. This facilitates their migration, potentially contributing to electrical conductivity or diffusion processes⁸¹.

Table 4.1 compares each crystal's and elementary phase's experimental values with the results obtained from three different functionals, *PBE*, *SCAN*, and *HSE06*. These functionals were used to study Na_3Sb and its elemental phases (Na and Sb). For Na, the lattice parameter value obtained by PBE was very close to the experimental value (3.767 Å), with a difference of only 1.06%. However, both SCAN and HSE06 showed no improvement compared to PBE, with HSE06 showing a variation of 1.72%. On the other hand, PBE provides a better approximation for Sb, with a difference of only 0.18% concerning the experimental value. Similarly, for Na_3Sb , PBE was the better approach, with a variation of 0.18%, consistent with the above tendency.

After deducting the total energy of free atoms from the total energy of the crystal unit cell, we found that the formation energy of Na_3Sb yields very similar results

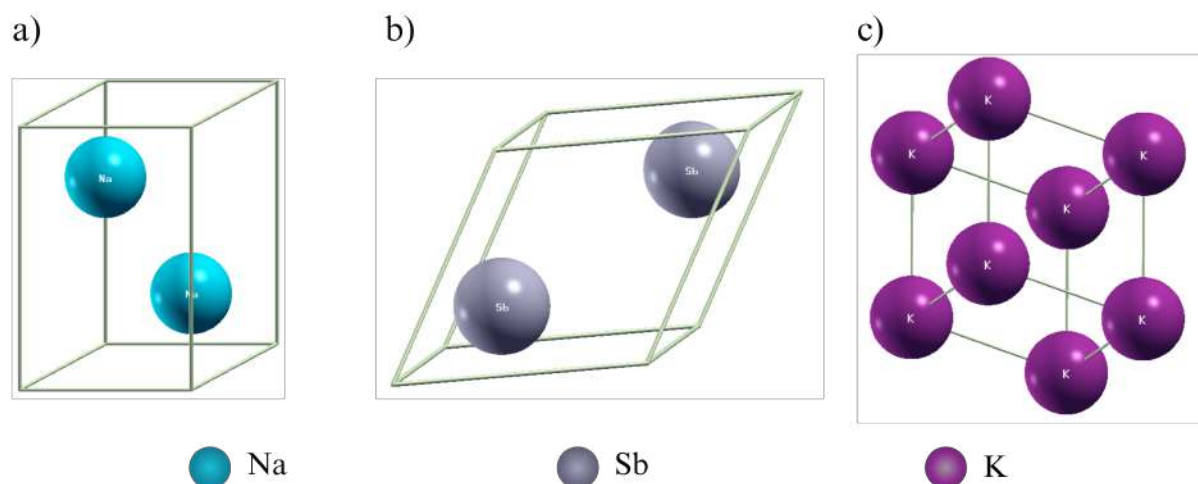


FIGURE 4.1: Ball and stick representation of the primitive unit cells of (a) Na, (b) Sb, and (c) K. Plots produced with the visualization software XCrystDen⁸².

for both the SCAN and the HSE06 functionals, with the former having slightly more negative value accordingly, PBE underestimates the cohesive energy by 14.14%. Since *HSE06* is computationally expensive, we decided to use SCAN as the preferred functional for the subsequent calculations on Na_2KSb and NaK_2Sb .

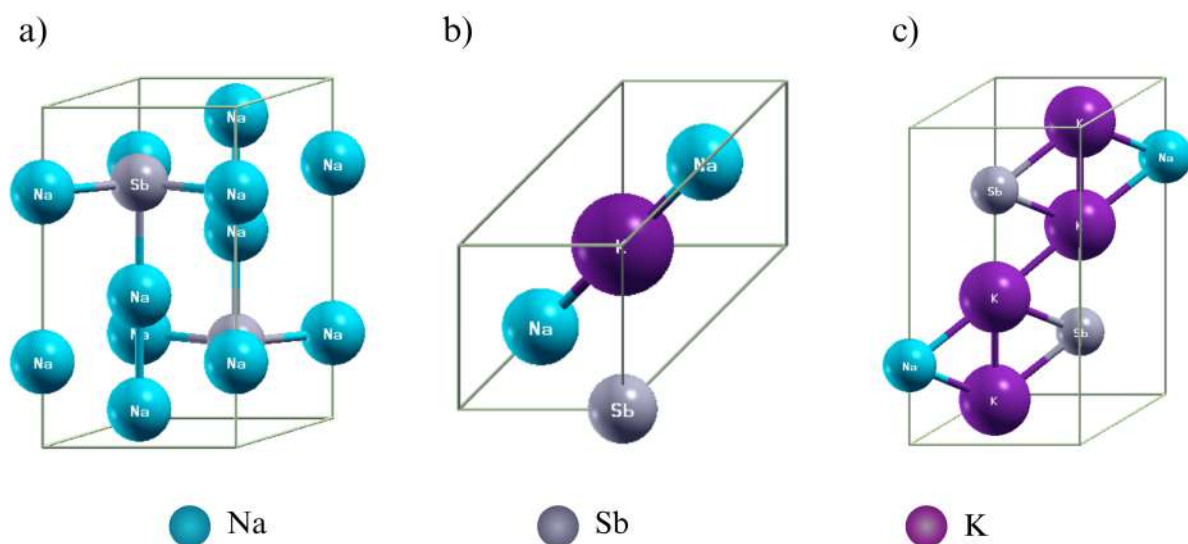


FIGURE 4.2: Ball and stick representation of the primitive unit cells of (a) Na_3Sb , (b) Na_2KSb , and (c) NaK_2Sb . Plots produced with the visualization software XCrystDen⁸².

In general, the positions of the atoms in the Na_3Sb structure are as follows: two atoms of Sb are located at $(1/3, 2/3, 1/4; 2/3, 1/3, 1/4)$, two atoms of Na_1 are located at $(0, 0, 1/4; 0, 0, 3/4)$, and four atoms of Na_2 are located at $(1/3, 2/3, 7/12; 2/3, 1/3,$

Crystal	Lattice Parameter	Functional			
		PBE	SCAN	HSE06	Exp
Na	a Å	3.763	3.763	3.832	3.767 ^a
	c Å	6.052	6.006	06.09	6.154
	Ω (Å ³ /atom)	37.110	36.301	38.740	37.117
Sb	a Å	4.585	4.219	4.648	4.501 ^a
	Ω (Å ³ /atom)	31.681	26.328	31.788	32.133
Na ₃ Sb	a Å	5.365	5.170	5.349	5.355 ^b
	c Å	9.540	9.168	9.510	9.496
	Ω (Å ³ /atom)	29.718	26.553	29.439	15.721
	E_{form}	-0.449	-0.542	-0.521	

^a [83] ^b [84]

TABLE 4.1: Lattice parameters, volume per atom (Ω), and formation energy per atom (E_{for}) of the conventional unit cell of Na, Sb and Na₃Sb

1/12; 1/3, 2/3, 11/12; 2/3, 1/3, 5/12)⁸³. Substituting one Na atom by K in Na₃Sb to form Na₂KSb leads to a stable cubic phase⁶⁴. In Na₂KSb, each atom in this compound is surrounded by eight nearest neighbors, forming a cubic coordination. Sodium atoms have four Sb and four K atoms as their nearest neighbors⁸³. K atoms are octahedrally coordinate by Sb atoms. On the other hand, the structure of Na₃Sb is much less symmetrical compared to Na₂KSb. The cubic form of Na₂KSb is because the distances between Na-Sb ($d=3.34$ Å) and K-Sb ($d=3.86$ Å) are closer to the ideal distance than what would be found in the Na₃Sb structure⁸³.

NaK₂Sb is a compound with a hexagonal arrangement of antimony atoms. Each antimony atom is surrounded by eleven alkali metal atoms⁴². The distances between the antimony and the alkali metal atoms are different for each type of bond. There are three types of bonds: Na-Sb bonds with a distance of 3.24 Å⁸⁷, K-Sb bonds with a distance of 3.64 Å, and $d_3 = 3.72$ Å. The coordination of the alkali metal atoms by antimony atoms can be of two types: planar triangular with d_1 bond length and a distorted tetrahedron of d_2 and d_3 bonds⁸³.

Crystal	Lattice Parameter	Functional	
		SCAN	Exp
K	a Å	6.627	5.321 ^a
	Ω (Å ³ /atom)	277.649	
NaK ₂ Sb	a=b Å	5.683	5.610 ^b
	c	11.211	10.932 ^b
	Ω (Å ³ /atom)	39.179	44.287
	E_{form} (eV/atom)	-7.321	
Na ₂ KSb	a Å	5.391	5.440 ^c
	Ω (Å ³ /atom)	27.693	26.170
	E_{form} (eV/atom)	-7.741	

^a [85] ^b [84] ^c [86]

TABLE 4.2: Lattice parameters, volume per atom (Ω), and formation energy per atom (E_{for}) of the conventional unit cell of K, NaK₂Sb, and Na₂KSb.

The lattice parameters of this crystal structure were calculated using SCAN, following the results obtained for Na₃Sb and its elemental phases. SCAN underestimated the value of the lattice parameter of K by 2.25%, NaK₂Sb by 1.3%, and for Na₂KSb, there is an underestimation of 0.9%. The best agreement with experiments is obtained with SCAN functional; similar results were obtained by other works^{22,23,25,60,88}, which demonstrate the consistency of our data, showing the superiority of SCAN functional over PBE in the prediction of formation energies.

4.2 Electronic Properties

4.2.1 Band Structure and Density of States

To comprehend the behavior of the materials as photocathodes, we analyze their electronic structure. This analysis involves an examination of the band structure and the density of states (DOS), which are further dissected into contributions from individual atoms. As shown in Figure 4.6 (a), the highest occupied states of Na₃Sb are primarily influenced by nondegenerate Sb electrons in the 5p-shell. This results

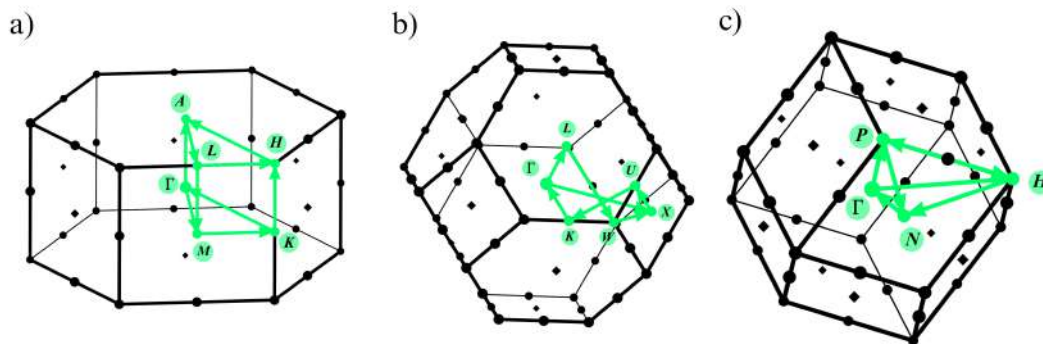


FIGURE 4.3: Illustrated in the graphics are the high-symmetry points and the path connecting them in the Brillouin zones of Na, Sb, and K. These graphics were created using XCrysDen

82

in the formation of six bands, with the lowest energy and limited variation, suggesting that these electrons are confined and provide only a modest contribution to the bonding.

The energy dispersion of Na-3s states exhibits considerable dispersion in all directions in k-space, with its energy minimum slightly above Γ . This minimum energy corresponds to the conduction band. The location exhibits a significantly reduced density of states in the DOS. This dispersion could be related to a delayed optical absorption onset, around 0.9 eV, which is the point where the material starts to absorb light. The Na-3p and Sb-5d states exhibit high energy levels. As a result, the absorption of phonons in the optical region is mostly influenced by the transitions from Sb-5p to Na-3s. The points in reciprocal space and the first Brillouin Zone are drawn in Figure 4.5 a. The band gap obtained for this system is shown in Table 4.3, Na₃Sb has a direct band gap. In the Table, PBE underestimates 63% compared to the experimental values reported. SCAN and HSE06 showed an error of 11% and 15.82%. Showing the superiority of SCAN in electronic properties calculations. These results are in good agreement with other theoretical calculations, where this crystal was reported as n-type conductivity^{64,65,87,89}.

Figure 4.6 shows the band structure and density of states (DOS) of the compound Na₂KSb. Figure 6.1 (b) illustrates the high symmetry points in the first Brillouin zone of reciprocal space corresponding to the compound. The valence band is primarily composed of Sb-5p states. It is evident that near the Γ point, three degenerate Sb-5p levels exhibit the highest energy level (valence band maximum). The conductive band exhibits its lowest energy state near the Γ point. The Na-3s and K-4s states significantly influence this region. The remaining conduction bands consist of Sb-d

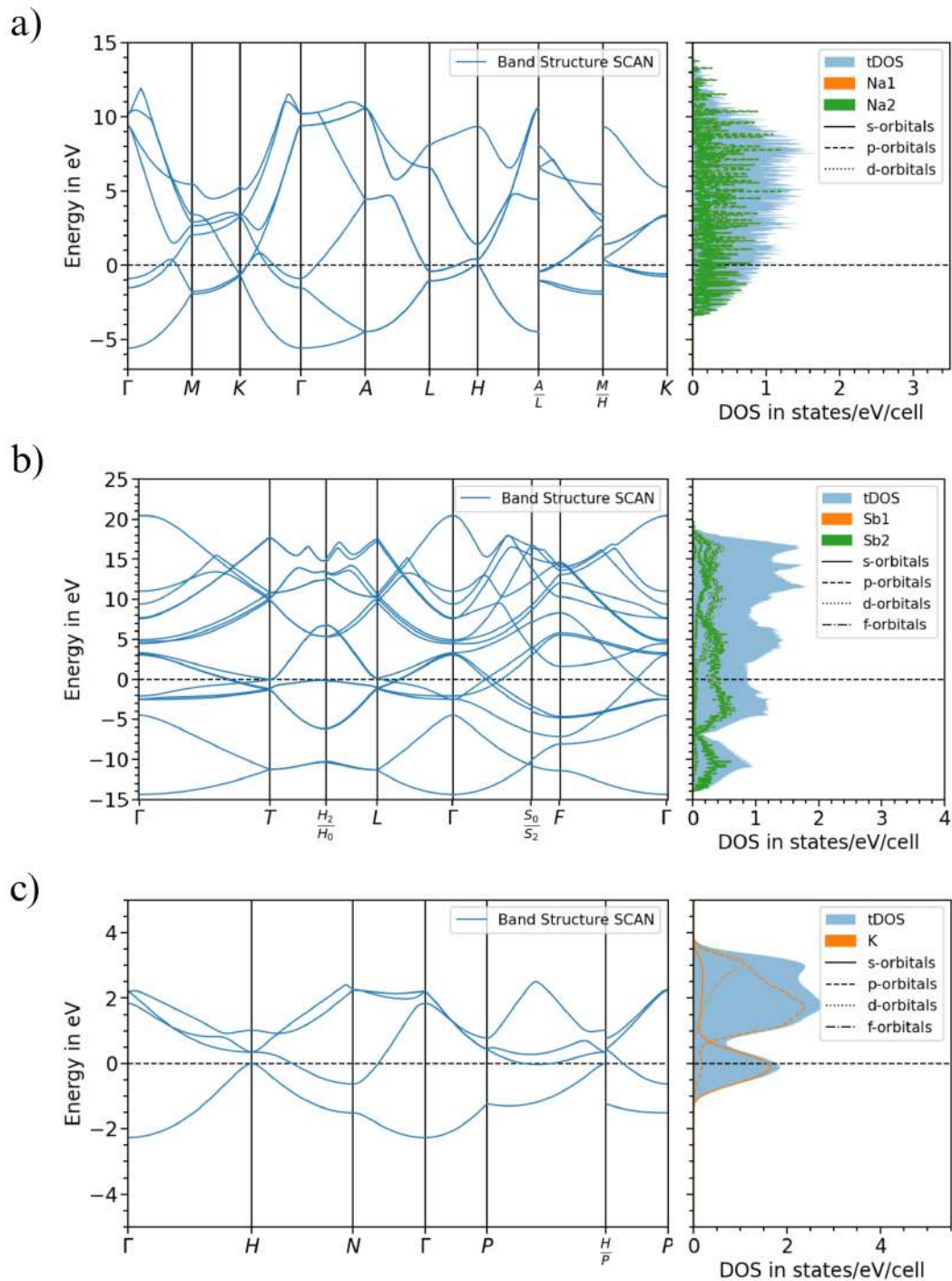


FIGURE 4.4: Band structure and PDOS of elemental phases (a) Na, (b) Sb, and (c) K using SCAN functional. The energy is referenced to the valence band maximum with a dashed line.

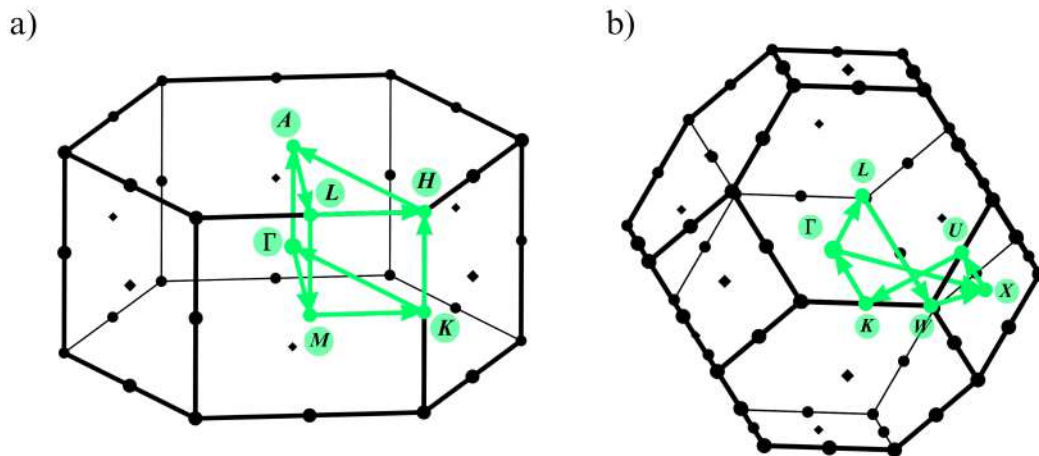


FIGURE 4.5: Illustrated in the graphics are the high-symmetry points and the path connecting them in the Brillouin zones of Na_3Sb and Na_2KSb . These visuals were created using XCrystDen⁸².

states and K. The band gap for this crystal structure is displayed in Table 4.6, with a magnitude of 1.526 eV. This number exhibits an overestimation of 52.6%, significantly higher than the values given by Etemma. Etemma's density of states calculation yielded a band gap of 1.4 eV⁶⁴. The conduction-band minimum of this material possesses greater energy than Na_3Sb , which can be attributed to the behavior of electrons. When electrons are excited to the conduction band, they encounter a reduced escape barrier. This makes it easier for them to be emitted from the solid, resulting in an increased photoemission current. The minimum point observed at X exhibits a hybridized character mainly involving Na-s states and Sb and K-d states⁶¹.

The K and Sb-d bands fall within the range of optical transitions in the blue and ultraviolet regions of the spectrum. Electrons that are stimulated to move to the conduction bands in Na_2KSb encounter a significantly lower obstacle in surpassing the vacuum level (electron affinity) compared to electrons that can return to lower energy levels immediately above the valence band by the emission of phonons, as observed in the mono alkali antimonide (Na_3Sb)³¹, the reported conductivity type for this crystal is p-type⁸⁷, which have a direct implication of the energy affinity behavior, due to the band's tendency to turn downward at the surface³¹.

NaK_2Sb is characterized by a direct band gap at Γ (Figure 4.6 c); here, it can be observed that Sb-p states dominate the valence band. Additional contributions from Na and K-p orbitals dominate the conduction band. Sb and Na-s states are found in lower energies, with a more dispersive shape of bands, highlighting the parabolic shape of the conduction band minimum (CBm) with a dominant contribution from

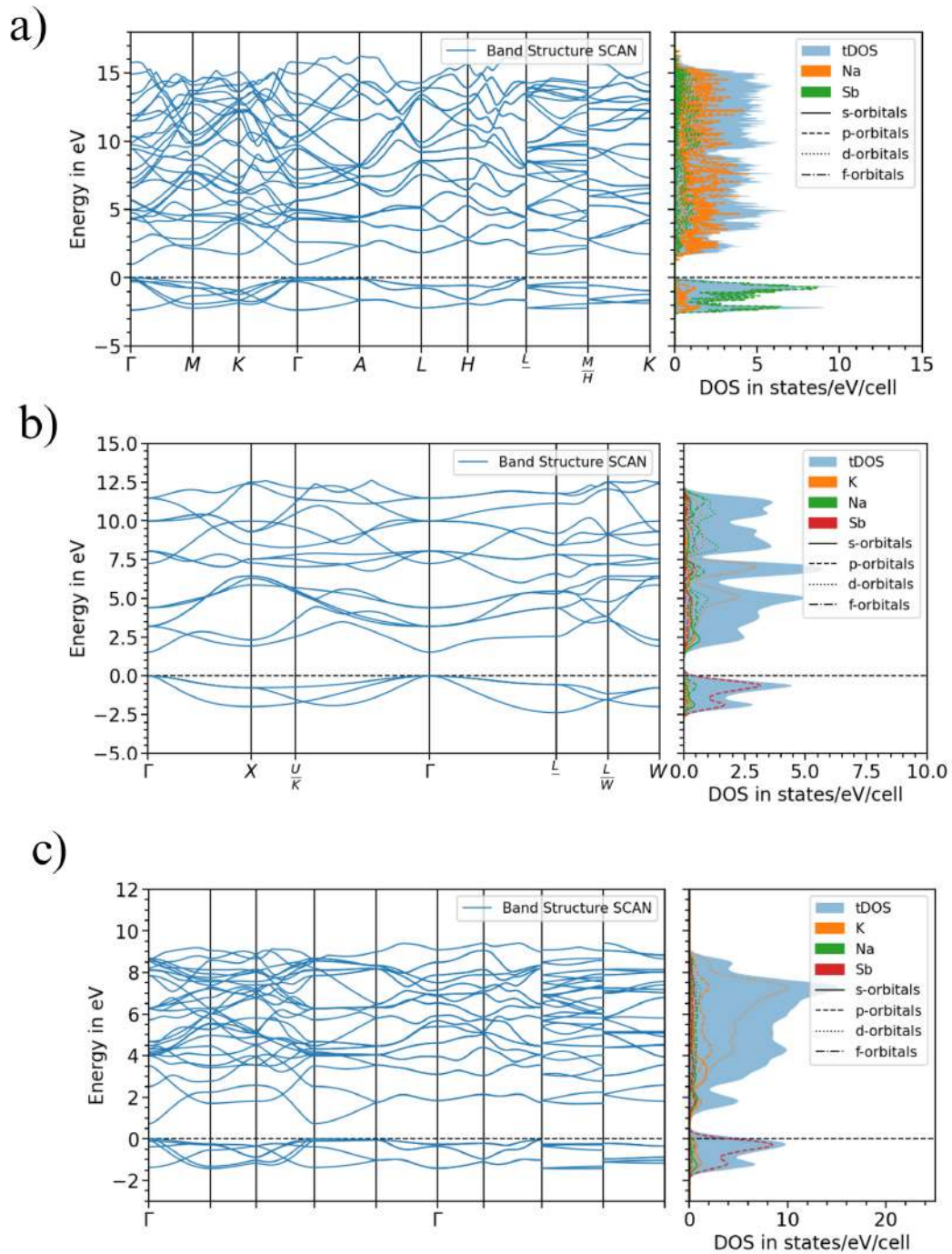


FIGURE 4.6: Band structure and PDOS of the different bulks: (a) Na_3Sb , (b) Na_2KSb , and (c) NaK_2Sb using SCAN functional. The energy is referenced to the valence band maximum with a dashed line.

Crystal	Band Gap	Functional			
		PBE	SCAN	HSE06	Exp
Na	E _{gap} (eV)	0.035	0.038	0.062	0,000 ^a
	E _{gap} +SOC (eV)	0.031	0.038	0.062	
Sb	E _{gap} (eV)	0,013	0.001	0.002	0.022 ^b
	E _{gap} +SOC (eV)	0.012	0.000	0.060	
Na ₃ Sb	E _{gap} (eV)	0,407	0.979	0.933	1.100 ^c
	E _{gap} +SOC (eV)	0.201	0.777	0.734	

^a [14] ^b [83] ^c [84]

TABLE 4.3: Electronic gaps including SOC effect corresponding to Na, Sb, Na₃Sb in eV.

Sb-s state and a minor way from Na and K. The bands directly above the CBm in the conduction region primarily contain Sb and s-like contributions. Here, the conduction bands above the CBm are mostly influenced by the hybridized sp-orbitals of the alkali atoms (Na and K), as shown in Figure 4.6 (c). The results using SCAN functional gave an underestimation of 33%. An early theoretical work based on the inclusion of QP correction reported a value of 0.96 eV and 0.44 eV using PBE as functional⁶¹.

When we compare different crystals, we find that Na₂KSb has a higher symmetry structure, leading to more regular coordination polyhedra⁴². Additionally, the Na-K bond distances are much shorter in Na₂KSb compared to NaK₂Sb, and they occur with greater frequency⁸⁴. Although Na₃Sb has a bandgap that could provide higher sensitivity in some detector applications, its narrow bandgap makes it susceptible to radiation damage, thus limiting its tolerance to high-intensity beams. However, Na₂KSb has a higher bandgap and could provide better radiation resistance than Na₃Sb, making it a more viable option for beams with higher intensities²⁹. It is also important to notice how the addition of K helps reduce the band gap, taking as reference Na₃Sb, showing a decrease of as reference 24.74%. DOS also shows how the Na-K contribution differs in each bulk, where NaK₂Sb has more of a contribution of K for conduction properties.

Crystal	Band Gap	Functional	
		SCAN	Exp
K	E _{gap} (eV)	0.005	0,000 ^b
	E _{gap} +SOC	0.005	
Na ₂ KSb	E _{gap} (eV)	1.526	1.000 ^a
	E _{gap} +SOC	1.313	
NaK ₂ Sb	E _{gap} (eV)	0.734	1.000 ^c
	E _{gap} +SOC	0.548	

^a [90] ^b [64] ^c [64, 91]

TABLE 4.4: Electronic gaps including SOC effect corresponding to K, Na₂KSb, NaK₂Sb in eV.

4.2.2 Spin Orbital Coupling Effect

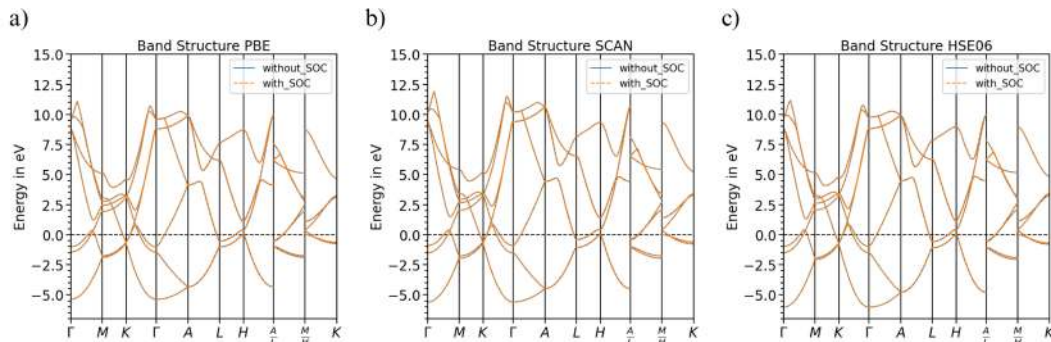


FIGURE 4.7: Computed band structures of Na using (a) PBE, (b) SCAN, and (c) HSE06 functionals with and without SOC. The valence band maxima without SOC correction are set to zero. Solid and dashed lines represent with and without SOC, respectively.

After performing the Electronic calculations, the Spin-Orbital Coupling (SOC) effect was incorporated into the calculations. Table 4.3 summarizes the numerical band gap results obtained for Na, Sb, and Na₃Sb using PBE, SCAN, and HSE06 functionals, with and without considering spin-orbit coupling. It is well-known that the SOC effect is not visible in sodium, where the only difference is apparent in the PBE functional, which is known for its poor ability to predict the electronic properties of materials (Figure 4.7). When subject to SOC, the band gap of Sb undergoes a significant change, with the band splitting magnitude ranging from 0.0009 eV to 0.054 eV for the SCAN and HSE06 functionals, respectively (Figure 4.8). The significant

variances are noticed at the high symmetry points T , L , and F in the SCAN spectra. As mentioned in the Methodology section, these outcomes were anticipated for materials such as Sb because of the SOC impact in its d-shell.

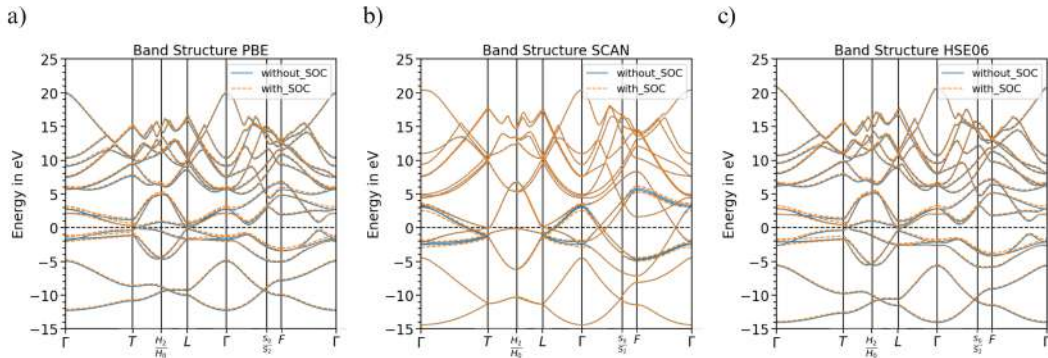


FIGURE 4.8: Computed band structures of Sb using (a) PBE, (b) SCAN, and (c) HSE06 functionals with and without SOC. The valence band maxima without SOC correction are set to zero. Blue solid and orange dashed lines represent with and without SOC, respectively.

In Na_3Sb , the band splitting magnitude ranges from approximately 0.2 eV in each functional, as expected for this type of material compared to others at the same level of theory^{61,92}. The shift can be observed in Figure 4.9 throughout the spectra, with an upward shift at all high-symmetry points, resulting in a reduction of the band gap by approximately 0.2 eV, as seen in Table 4.3. When comparing the exchange-correlation functional, a significant difference is the fixed displacement of the conduction bands, which leads to an increased band gap in all materials.

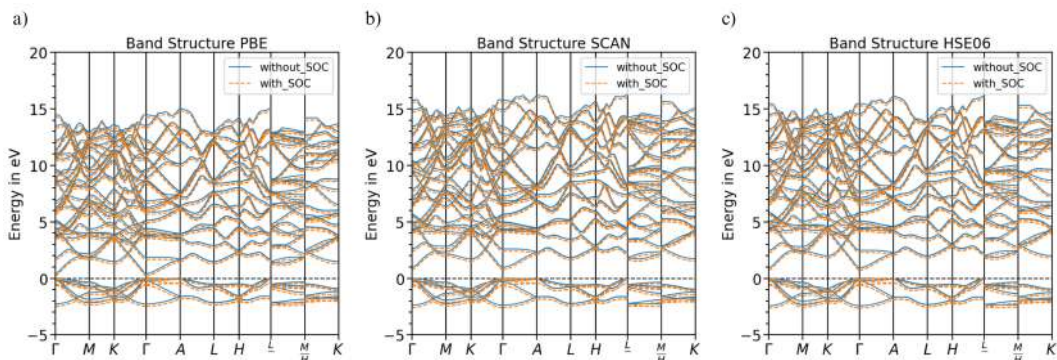


FIGURE 4.9: Computed band structures of Na_3Sb using (a) PBE, (b) SCAN, and (c) HSE06 functionals with and without SOC. The valence band maxima without SOC correction are set to zero. Blue solid and orange dashed lines represent with and without SOC, respectively.

In Figure 4.10 (a), it was anticipated that there would be no splitting in the material K. In the case of Na_2KSb , however, as shown in Figure 4.10 (b), bands split all over the high-symmetry points. This is especially clear in the valence region and around the high-symmetry points. The magnitude of the band splitting at Γ is approximately 0.22 eV, a value similar to that of Na_3Sb . Finally, for NaK_2Sb , SOC splitting is more notorious in all of the high-symmetry points (Figure 4.10 (c)). Again, the valence band maximum is shifted upwards at Γ , reducing the band gap by about 0.2 eV (Table 4.4). The spin-orbit coupling (SOC) effect affects the occupied bands much more strongly than the unoccupied ones in all materials. Our findings are consistent with the trend demonstrated in previous theoretical studies. All functionals taken into consideration recreate these effects in nearly identical ways; nevertheless, the description of this feature is affected far more strongly by approximations in the handling of relativistic effects than by the one on v_{xc} ⁹².

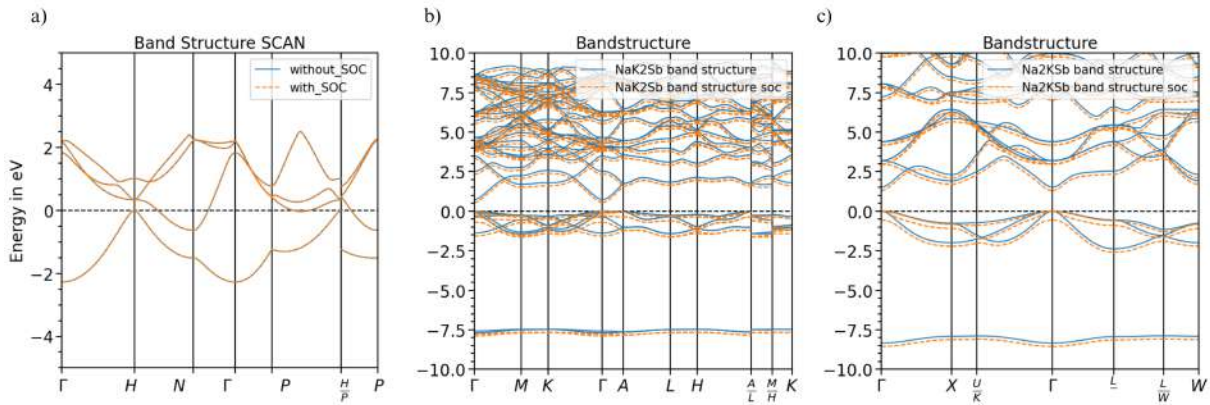


FIGURE 4.10: Computed band structures of (a) K, (b) NaK_2Sb , and (c) Na_2KSb . The valence band maxima without SOC correction are set to zero. Blue solid and orange dashed lines represent with and without SOC, respectively.

4.3 Optical Properties

4.3.1 Dielectric Function

4.3.1.1 Elemental Phases

Na, Sb, and K are well known for their metallic character. In the case of Na, Figure 4.11 illustrates the distinct material responses depending on crystallographic directions. Specifically, the xx and yy directions exhibit a response that differs from the zz direction. We use the PBE functional to identify the first peak (for the xx direction)

in the imaginary part (ϵ_2) at 1.2 eV, representing the highest absorption. The peak intensity was recorded at 0.27. Following this are smaller peaks at 2.3, 3.1, and 4.2 eV. In contrast, the zz direction exhibits its initial peak at 2.3 eV, along with a shoulder at 3.1 eV and smaller peaks at 4.2, 4.9, 5.6, and 7.8 eV.

A similar anisotropic behavior is evident when the real part (ϵ_1) is examined. A principal peak at 1 eV follows the xx and yy directions with an intensity of 1.0, while the zz direction displays its principal peak at 2.3 eV at 0.4 at $Im[\epsilon(\omega)]$ scale. Both directions exhibit a negative peak, indicative of a plasmon resonance response typically expected in metals like Na. When comparing the SCAN and HSE06 functionals, we observe similar peak positions but different absorption behaviors. The SCAN functional displays more prominent peaks, while the HSE06 functional behaves similarly to PBE but with slightly enhanced absorption.

Anisotropy is noticeable in Sb due to its varied responses in different directions. ϵ_2 exhibits a principal peak at 0.3 eV in the xx direction, with a shoulder at 0.6 eV. In the yy direction, the peak overlaps with the shoulder of the xx peak at approximately 0.6 eV. The response in the zz direction shows less absorption with a set of peaks from 0.9 to 2.3 eV. When using SCAN, we observe changes in peak intensity. The zz direction shows greater absorption than xx , and the yy direction exhibits a less broadening character and less absorption. HSE06 shows a major change in the zz response, with a principal peak at 3.3 eV and a smaller one at 1.7 eV. All peaks have lower absorption than PBE and SCAN, as shown (Figure 4.12). Regarding ϵ_1 , we can see that PBE has a similar behavior in the xx and yy directions, with the main peak occurring at 0.3 eV. In the zz direction, the peaks are not as well-defined as in the other directions but show prominence at 0.5 and 1.6 eV. With SCAN and HSE06, we observe a similar behavior to the imaginary part, where the absorption values change between directions but maintain a comparable pattern. The plasmon resonance response is also visible at negative absorbance values.

The spectra of element K exhibit a similar anisotropic behavior to the other elemental phases, as shown in Figure 4.13. The imaginary part of the spectra displays a primary peak at 5.8 eV, with six smaller peaks at 1.7, 2.3, 3.1, 3.9, 5.2, and 6.5 eV. Similarly, ϵ_1 exhibits a set of peaks, with the primary ones at 1.2 and 2.3 eV.

For metals like Sodium (Na) and Potassium (K), we would expect ϵ_1 of the real part of the dielectric function to be very low or even negative due to their electrons being very mobile due to its response quickly to an electric field, producing high

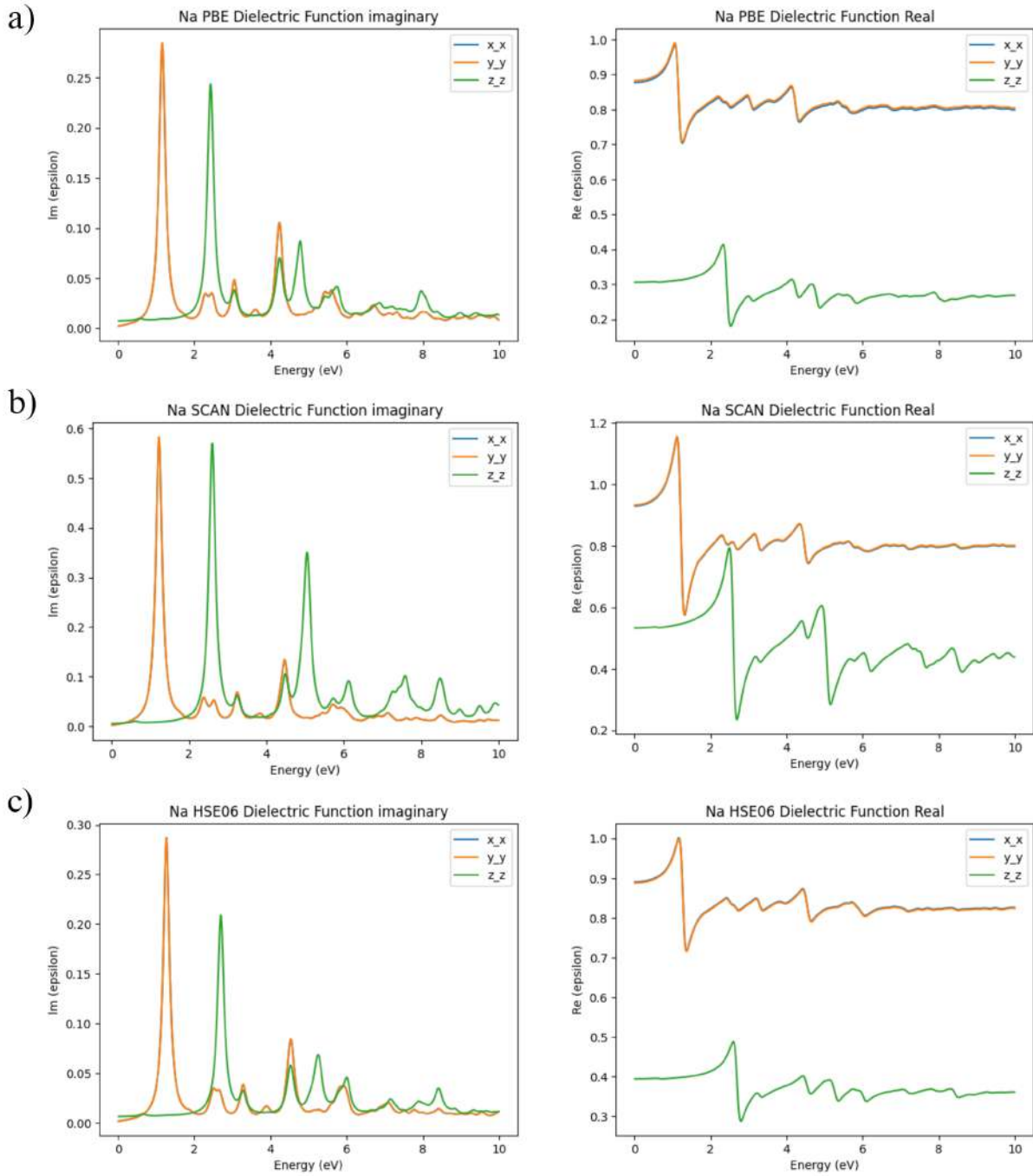


FIGURE 4.11: Imaginary and real part of the dielectric functions corresponding to Na with different functionals: (a) PBE, (b) SCAN, and (c) HSE06.

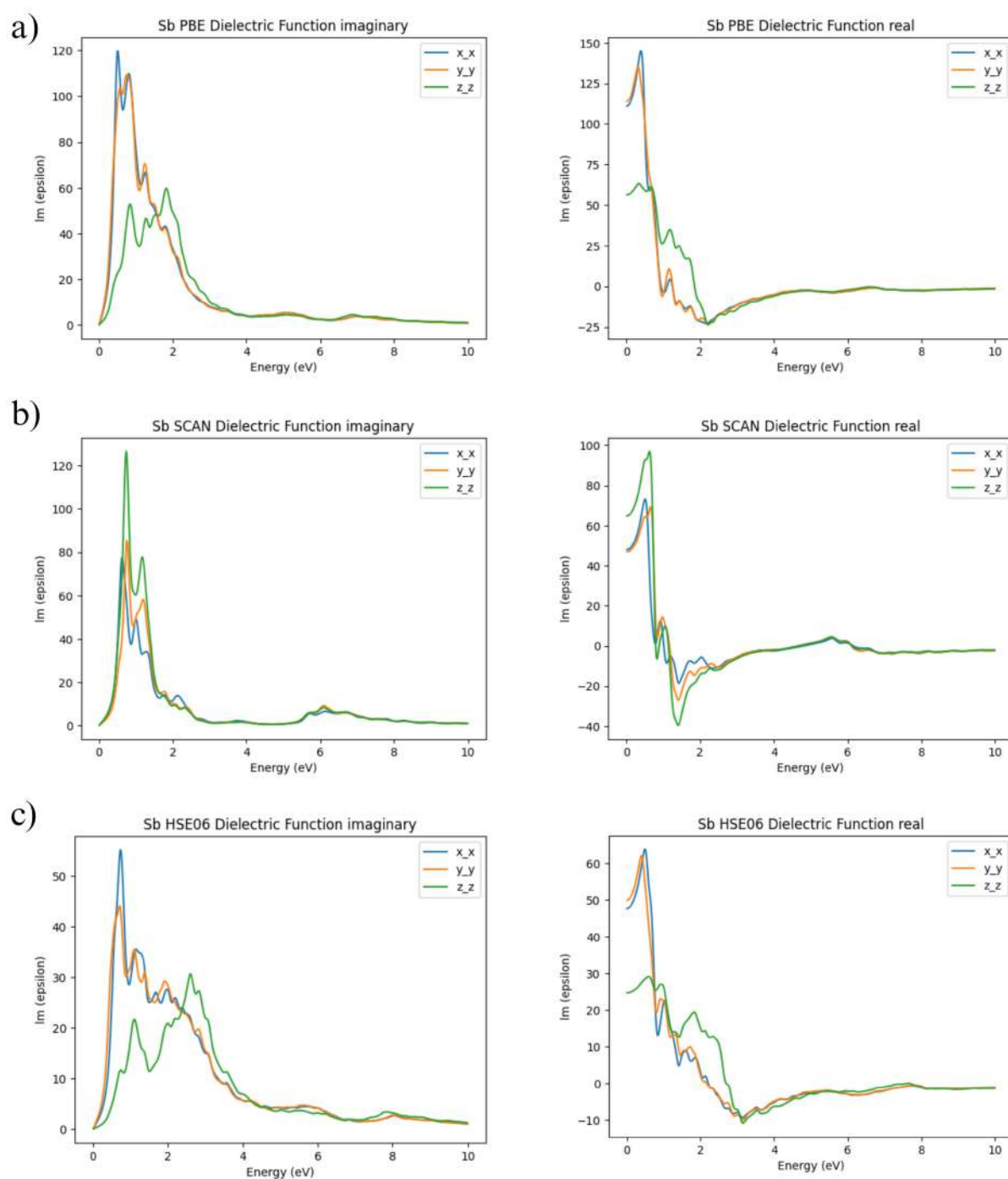


FIGURE 4.12: Imaginary and real part of the dielectric functions corresponding to Sb with different functionals: (a) PBE, (b) SCAN, and (c) HSE06.

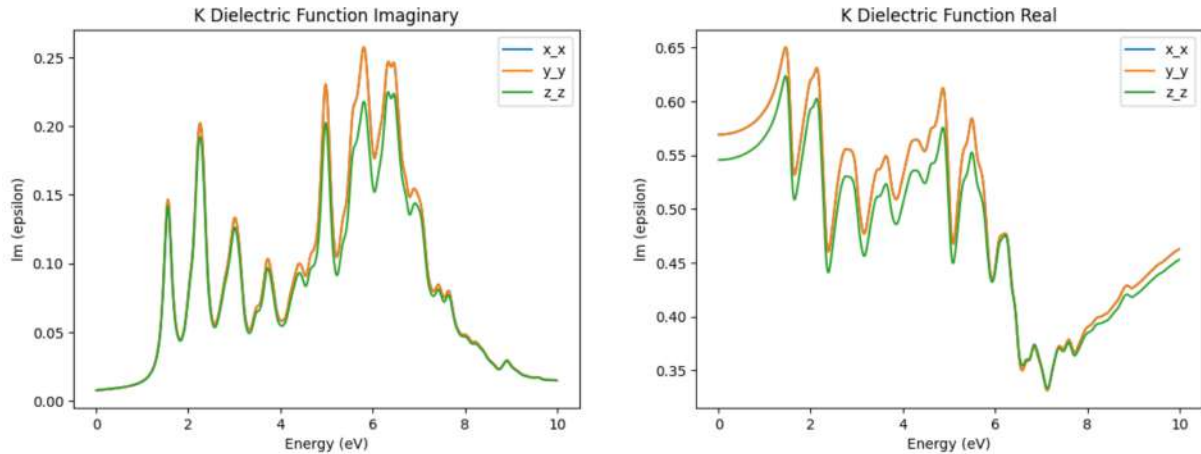


FIGURE 4.13: Imaginary and real part of the dielectric functions corresponding to K using SCAN as functional.

electrical conductivity. The low permittivity indicates that metals allow easy passage of electric currents. When examining ϵ_2 , it is typical to observe that free electron movement accounts for most electrical conduction in metals and that the imaginary part does not lose much energy compared to dielectric materials. Regarding metalloids like Antimony (Sb), we can anticipate a dielectric response between metals and non-metals. Metalloids' real permittivity is not expected to be as low as metals due to their lower electrical conductivity, but they also will not be as high as insulators. ϵ_2 may be more noticeable than metals, yet still lower than many dielectric materials. This suggests that the material has some capacity to store electrical energy, although not as efficiently as pure dielectric materials.

4.3.1.2 Multi-Alkali Antimonides

After examining the dielectric function of hexagonal Na_3Sb (Figure 4.14), it was noticed that the xx and yy directions have a similar pattern. In contrast, the zz direction slightly differs from the other two directions. This can be attributed to the hexagonal shape of the crystal, where the zz direction is perpendicular to the hexagonal plane, while the xx and yy directions are within the plane. The PBE method shows ϵ_2 where the primary peaks are found at 0.7 eV and 2.3 eV, with a shoulder at 2.5 eV and a smaller peak at 3.9 eV for the zz direction. The main peaks could be attributed to the transition between the highest-occupied Sb p -bands and the lowest-unoccupied Na s -bands at the M symmetry point. However, more advanced calculations are necessary to assign the specific electronic structure involved in this absorption peak. For the xx direction, the primary peak is observed at the same location as the zz shoulder, with similar peaks at 3.9 eV but with a difference in the

absorption response. When using SCAN and HSE06 methods, a displacement to the right direction is observed by a few units, with 2.6 and 2.9 eV being the principal peak values for the zz direction, respectively. ϵ_1 and ϵ_2 display similar behaviors regarding direction. The primary peak is observed at approximately 1.6-2 eV and a smaller peak at 3.3 eV, indicating the plasmon resonance response at negative absorption values. We can observe a similar response when using either SCAN or HSE06. There are slight differences in the shape of the peaks, but they both have peaks at 2.3 and 3.9 eV.

NaK₂Sb (Figure 4.16 (a)) exhibits different behavior in its anisotropy, but the directions show similar patterns. The most prominent peak is observed at 2.3 eV, accompanied by smaller peaks at 3.3 and 4.6 eV with indistinct shapes. The spectra display various shoulders and lack the desired resolution for our purpose. The main peak is likely associated with the transition between the highest-occupied Sb p -bands and the unoccupied K s -bands at the H symmetry point. In ϵ_1 , two peaks at 1.7 and 3 eV dominate, with some additional shoulders around 4.3 eV. In contrast, Na₂KSb (Figure 4.16 (b)) demonstrates isotropic characteristics. ϵ_2 reveals a primary peak at 3.3 eV, which can be attributed to the transition between the highest-occupied Sb p -bands and the unoccupied Na s -bands at the L/W symmetry point. The dominant feature in ϵ_1 of the data occurs at 2.6-2.8 eV, accompanied by a secondary peak at 4.3-5.2 eV.

Generally, for the materials under discussion, it is important to note that at low energies (below the bandgap), the real part (ϵ_1) should approach a high positive value, usually 10-20, indicating its electronic polarization. At the same time, the imaginary part (ϵ_2) stays close to zero within this energy range. As the bandgap energy (E_g) approaches, ϵ_1 is expected to decrease toward zero because fewer electronic states are available for transitions. At the bandgap energy, ϵ_2 shows a sharp peak, indicating light absorption that excites electrons from the valence band to the conduction band. Once the energy progressively approaches infinity, ϵ_1 will drop towards zero beyond the bandgap. In this domain, ϵ_2 is expected to show additional peaks and valleys corresponding to higher-energy interband transitions, which may involve intraband transitions with core electrons. Taking into account Na₃Sb: This compound has a smaller bandgap (near 0.9 eV) than both Na₂KSb and NaK₂Sb (about 1.1 eV), so the peak in ϵ_2 for Na₃Sb will occur at a lower energy than the other two materials. Comparing Na₂KSb and NaK₂Sb: These compounds have similar bandgaps, indicating their ϵ_2 peaks should align at similar energies. Nevertheless, differences in their band structures and the oscillator strengths of transitions

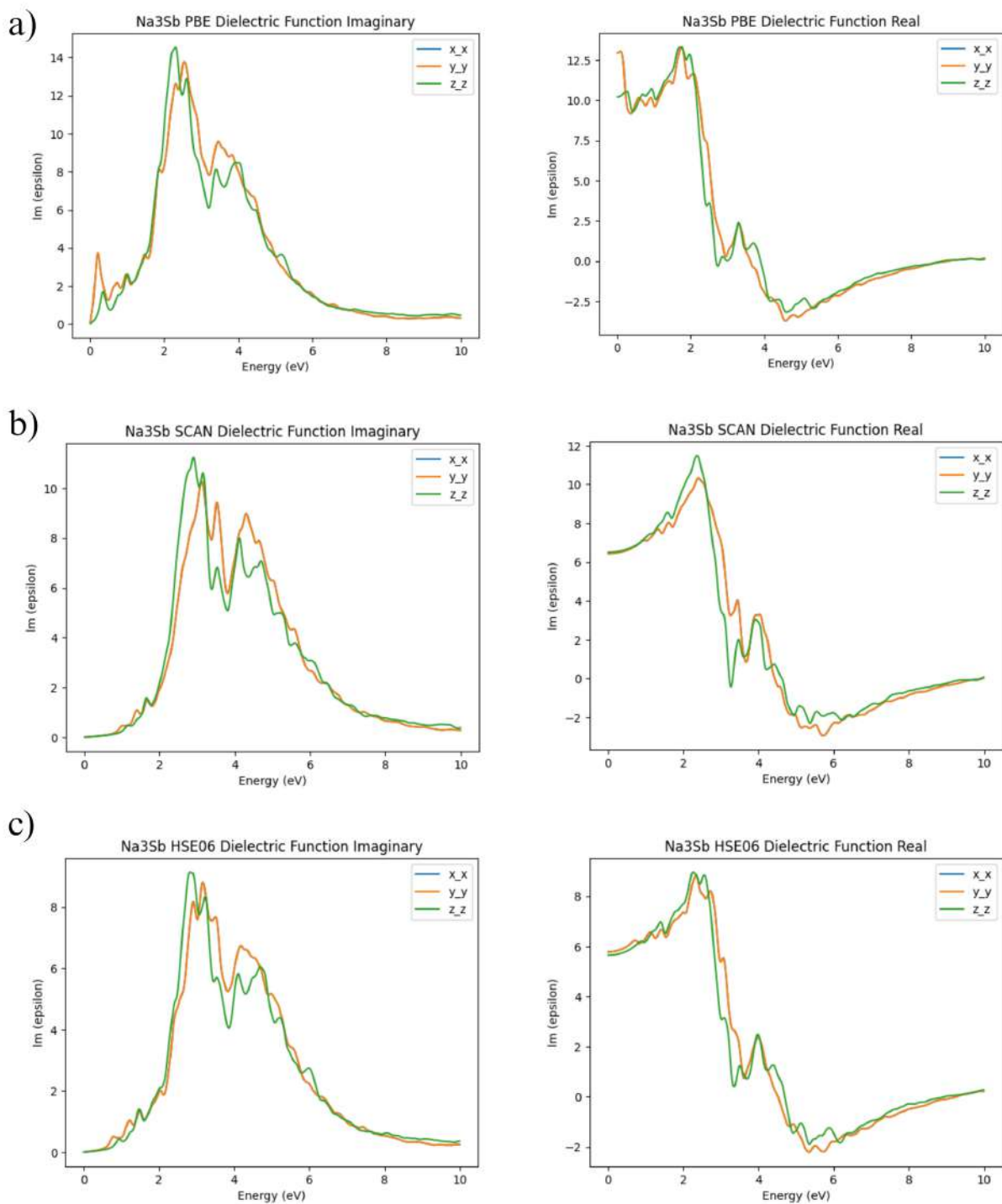


FIGURE 4.14: Imaginary and real part of the dielectric functions corresponding to Na₃Sb with different functionals: (a) PBE, (b) SCAN, and (c) HSE06.

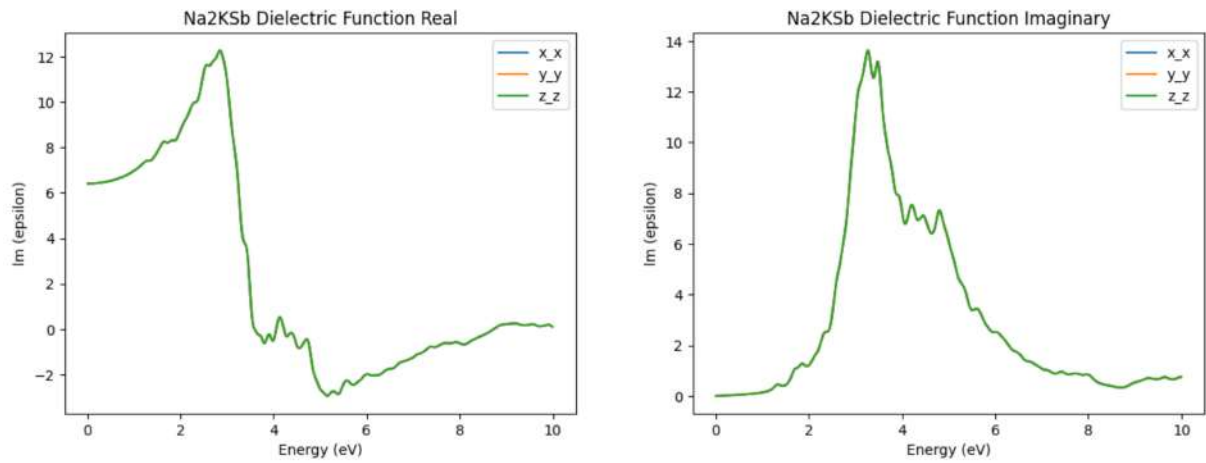


FIGURE 4.15: Imaginary and real part of the dielectric functions corresponding to Na₂KSb using SCAN functional.

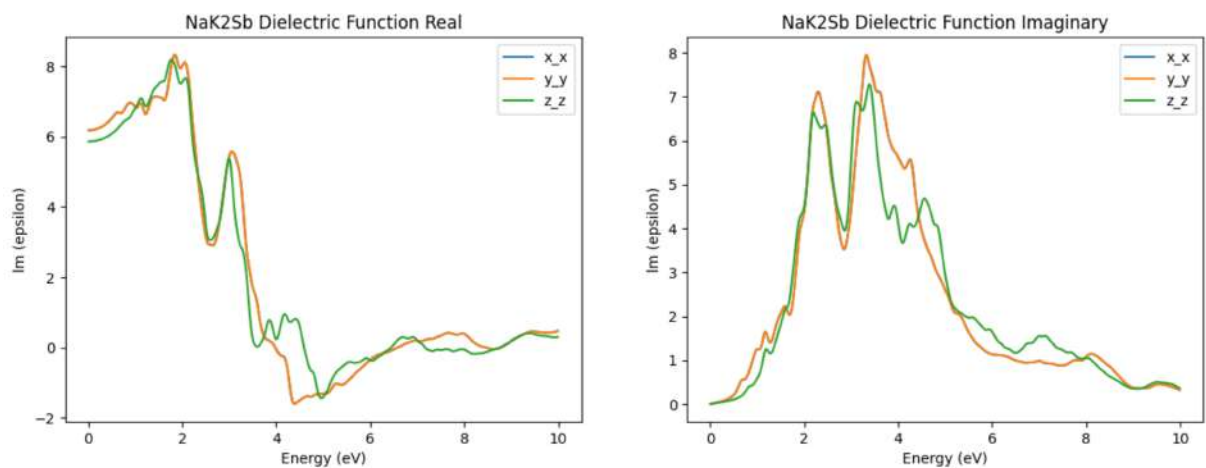


FIGURE 4.16: Imaginary and real part of the dielectric functions corresponding to NaK₂Sb using SCAN functional.

could lead to variations in the relative intensities of these peaks.

It is important to note that the dielectric properties of materials are significantly affected by the frequency of the electric field applied to them⁷⁰. At frequencies below 1 MHz, the dielectric properties are mainly influenced by ionic conductivity and electronic polarization, resulting in high dielectric constant values due to their ionic nature. Electronic polarization dominates at higher frequencies exceeding 1 GHz, decreasing the dielectric constant with increasing frequency. For practical applications, a high value of the real part of the dielectric constant (ϵ_1) at lower frequencies is desirable, indicating strong electronic polarization³⁵. On the other hand, for the imaginary part of the dielectric constant (ϵ_2), it is better to have well-defined peaks near the bandgap due to the significance of light absorption for electron excitation. Peaks and valleys at higher energies may correspond to further interband and intraband transitions. The anisotropy of some materials may require careful alignment in optical setups⁹³. For instance, Na₃Sb, which has a lower bandgap with an earlier peak (0.7 eV), is potentially advantageous for low-energy applications. Meanwhile, Na₂KSb and NaK₂Sb exhibit similar ϵ_2 peak locations (around 2.3 eV), which could be attributed to a balance between sensitivity and response time for fast shutters. The isotropic nature of Na₂KSb simplifies the optical configuration of experimental setups. However, operating conditions such as beam intensity should also be taken into account³⁹.

4.4 Core-Level Spectroscopy

The following Tables report each state's calculated core level energies in all the investigated materials. Some values were left out of the Table because SOC did not affect them. We categorized the binding energies based on the principal quantum numbers n and identified the contributions from different Na atoms in Na₃Sb by their location in the Table's unit cell. Energy separation of 0.25-0.27 eV consistently separates the binding energies of core levels linked to crystallographically inequivalent Na atoms in Na₃Sb, with states concerning atoms on-site A₂ always being energetically deeper (Figure 4.17).

The value difference can be attributed to various factors for the 1s orbital of Na (Table 4.5). The first is the formal charge of the Na ion in each compound. Na₃Sb has the lowest formal charge (+1/3), while NaK₂Sb has the highest (+1). This influences the electrostatic attraction between the Na nucleus and the 1s electron. The

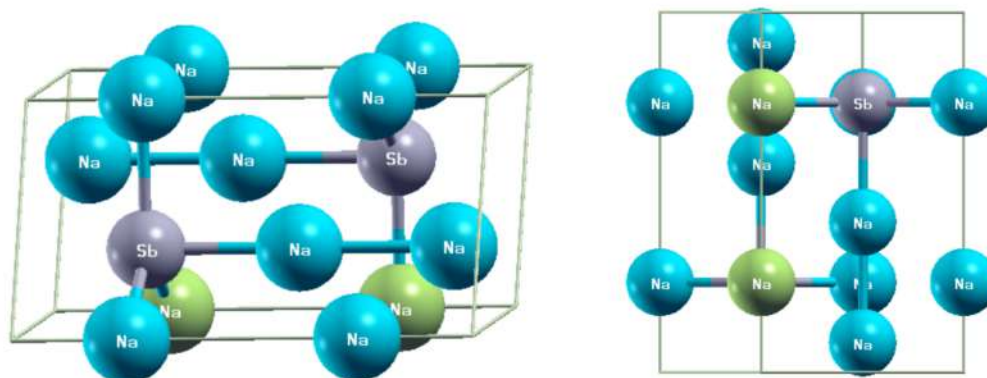


FIGURE 4.17: Ball and stick representation from different perspectives of the primitive unit cells of Na_3Sb , Na (A_1) atoms in blue light, Na (A_2) atoms in green, and Sb atoms in grey. Plots produced with the visualization software XCrysDen⁸².

	Na (A_1) 1s	Na (A_2) 1s	Sb 1s	K 1s
Na_3Sb	-0.77	-0.48	1.090	-
Na_2KSb	-1.270	-	0.800	-1.280
NaK_2Sb	-0.576	-	1.443	-0.670

TABLE 4.5: Core-level binding energies computed from DFT for 1s-orbital in Na_3Sb , Na_2KSb , and NaK_2Sb . Inequivalent Na atoms are identified based on their crystallographic sites. All values are expressed in electronvolts (eV).

charge distribution in the compound also has an impact on the binding energy. This is because the difference in electronegativity between the nearby atoms (Sb and K) changes the charge distribution around the Na ion. Second, hybridization is also an important factor. It is known that sp^3 hybridization in Na_3Sb and hexagonal NaK_2Sb creates orbitals with more directionality, which raises the 1s binding energy. Finally, the compact hexagonal geometry of Na_3Sb and hexagonal NaK_2Sb allows for greater orbital overlap, strengthening the 1s interaction. In conclusion, Na's 1s binding energy values reflect the influence of various factors intrinsic to the Na ion and the chemical environment in each compound.

	Na (A1) 2s	Na (A2) 2s	Sb 2s	K 2s
Na_3Sb	-0.810	-0.550	1.056	—
Na_2KSb	-1.320	—	0.780	-1.420
NaK_2Sb	-0.581	—	1.445	-0.753

TABLE 4.6: Core-level binding energies computed from DFT for 2s-orbital in Na_3Sb , Na_2KSb , and NaK_2Sb . All values are expressed in electronvolts (eV).

	Na 3s	Sb 3s	K 3s
Na₃Sb	—	1.092	—
Na₂KSb	—	0.800	-1.580
NaK₂Sb	—	1.500	-0.841

TABLE 4.7: Core-level binding energies computed from DFT for 3s-orbital in Na₃Sb, Na₂KSb, and NaK₂Sb. All values are expressed in electronvolts (eV).

	No SOC				SOC			
	Na (A ₁) 2p	Na (A ₂) 2p	Sb 2p	K 2p	Na (A ₁) 2p	Na (A ₂) 2p	Sb 2p	K 2p
Na₃Sb	-0.820	-0.570	1.059	—	-0.760	-0.640	1.061	—
Na₂KSb	-1.330	—	0.780	-1.400	-1.330	—	0.790	-1.400
NaK₂Sb	-0.590	—	1.444	-0.742	-0.590	—	1.448	-0.743

TABLE 4.8: Core-level binding energies computed from DFT for 2p-orbital in Na₃Sb, Na₂KSb, and NaK₂Sb. All values are expressed in electronvolts (eV).

The 1s binding energy of Sb in cubic Na₂KSb is significantly lower than in the other two compounds. This could be attributed to two different cations (Na and K) in the Sb environment, which generates a more complex electrostatic environment. The highest is the 1s binding energy of Sb in hexagonal NaK₂Sb. The compound's compact hexagonal geometry and sp^3 hybridization of Sb are the main factors contributing to this difference. We have values very close to Na for K, which makes sense considering the similarities in chemical environments and electrostatic implications. Table 4.6 shows that the energy of the 2s orbital drops by an average of 0.025 eV in Na energies. Energy levels for Sb and K are decreasing. This pattern is expected given that the binding energy of the 1s orbital is greater than that of the 2s orbital; higher binding energies correlate to lower levels. It is noteworthy to note that the values of hexagonal phases are closer than those of cubic crystals. In terms of the Sb orbitals, we discover that Na₃Sb and Na₂KSb frequently differ by 0.27-0.29 eV, while NaK₂Sb generally differ by 0.35-0.40 eV.

	No SOC		SOC	
	Sb 3p	K 3p	Sb 3p	K 3p
Na₃Sb	1.093	—	1.062	—
Na₂KSb	0.800	-1.650	0.810	-1.650
NaK₂Sb	1.500	-0.927	1.504	-0.920

TABLE 4.9: Core-level binding energies computed from DFT for 3p-orbital in Na₃Sb, Na₂KSb, and NaK₂Sb.

	No SOC			SOC		
	Sb 3d	Sb 4s	Sb 4p	Sb 3d	Sb 4s	Sb 4p
Na₃Sb	1.086	1.170	1.181	1.086	1.170	1.184
Na₂KSb	0.800	0.870	0.880	0.800	0.870	0.890
NaK₂Sb	1.492	1.602	1.616	1.492	1.602	1.621

TABLE 4.10: Core-level binding energies computed from DFT for Sb core levels orbital in Na₃Sb, Na₂KSb, and NaK₂Sb. All values are expressed in electronvolts (eV).

In the case of K, the difference ranges between 0.6 and 0.7 eV for all core orbitals. The states in Na₂KSb are deeper than those in NaK₂Sb. All atoms in Na₃Sb and NaK₂Sb have higher core binding energies than those in Na₂KSb by varying energy. The most significant alterations in core-level binding energies occur between the 1s and 2p states in the bi-alkali antimonides under consideration. The impact of SOC is primarily seen in the highest energy states such as 2p, 3p, and 4p. In the Na-2p shell, a splitting is observed in Na₃Sb of approximately 0.6 eV in (*A*₁) and 0.7 eV in (*A*₂). These values remain consistent in Na₂KSb and NaK₂Sb. For Sb, there is a slight increase in all energy levels, while for K, the energies remain relatively unaffected. This same pattern is observed for the 3p-shell. In the case of 4p, minimal variation is observed across all scenarios.

Chapter 5

Conclusions and future work

We have found that using the SCAN method is the best way to estimate the exchange-correlation potential in DFT calculations of Na-Sb phases. The PBE method is appropriate for simulating structural characteristics but is not recommended for accurately describing electrical properties. Compared to the widely used range-separated hybrid functional HSE06, SCAN produces better results regarding lattice vectors and unit-cell volumes in the studied materials. However, the HSE06 yields more accurate outcomes for electronic and optical gaps that are consistently closer to the experimental references. HSE06 is designed to accurately replicate band gaps using DFT, so it is expected to do so. Although HSE06 is normally more computationally expensive, SCAN is a more practical option for studying surfaces and defective bulk materials that require huge supercells. The effectiveness of SCAN in replicating the electrical characteristics of the Na-Sb-based materials under examination can be attributed to the orbital nature of the bands in the vicinity of the energy gap, where the valence and conduction regions of the crystals are influenced mainly by s- and p-orbitals. The GGA approximation already provides satisfactory results for these orbitals so that any meta-GGA implementation may be effective for these systems. However, the numerical performance can significantly vary based on the specific parameterization details and should be thoroughly evaluated.

Our study showcases the effectiveness of ab initio techniques in solid-state theory to reveal the underlying physical characteristics of photocathode materials. We have used advanced techniques like DFT to calculate the electronic properties of three alkali elements, specifically Na₃Sb, Na₂KSb, and NaK₂Sb. Regarding the lattice parameters and relaxation calculations, it was found that PBE shows a very good approximation of the experimental values reported, followed by SCAN. In the case of HSE06, it tends to overestimate the corresponding lattice parameters.

Our band gap analysis shows that all three systems have different band gaps, ranging from 0.734 eV in NaK₂Sb to 1.526 eV in Na₃Sb. The band gap character is direct at the Γ point in all three compounds. We found that antimony p states

mainly influence the valence bands. In contrast, the conduction bands have significant contributions from the s-states of sodium (Na) and potassium (K) states at lower energies and antimony d-states farther from the Fermi energy. The changes in binding energies of the central states linked to individual atomic species in specific crystallographic locations show consistent patterns. The most stable bulk is Na_2KSb , with a more negative E_{form} .

The dielectric function shows significant absorbance between 0.7 and 4 eV for the three compounds. Additionally, our modeling findings reveal significant displacements, around 0.6, 0.7, and 0.35 eV, for sodium (Na) s, potassium (K) 2p, and antimony (Sb) 3d energy levels when comparing Na_3Sb with the two other compounds. These patterns can be used to establish connections between theoretical predictions and experimental results on photocathode samples made of bi-alkali antimonide and XPS. As was expected, the SOC effect shows a principal impact in Sb-p orbitals and a minimal effect in the band gaps obtained (about 0.2 eV). Our research emphasizes the significance of employing ab initio theory in optimization. We have only explored the properties of ideal stoichiometric bulk materials using fundamental principles. Further research is required to connect these findings and experimental data.

We can conclude that NaK_2Sb exhibits a band gap of 0.73 eV that is more favorable towards photoemission effects due to better electronic transmission between CBm and VBm. Na_2KSb has a bandgap of 1.53 eV, indicating less favorable electronic transmission effects. Regarding dielectric properties, it is worth noting that NaK_2Sb may be more suitable for low-energy applications due to its lower bandgap with an earlier peak of 0.7 eV. Conversely, Na_2KSb and Na_3Sb have similar ϵ_2 peak locations (around 2.3 eV), which can be attributed to a balance between sensitivity and response time for fast shutters. The isotropic nature of Na_2KSb also simplifies the optical configuration of experimental setups. Adding K atoms shows a desired reduction effect (24.74%) in the bandgap, taking Na_3Sb as a reference. However, it is important to consider operating conditions such as beam intensity. From this perspective, the results of this study represent the first step in establishing a solid connection between the experimental preparation and characterization of photocathodes and the accurate prediction of their electronic structure.

Chapter 6

Annexes

6.1 Band Structures and DOS

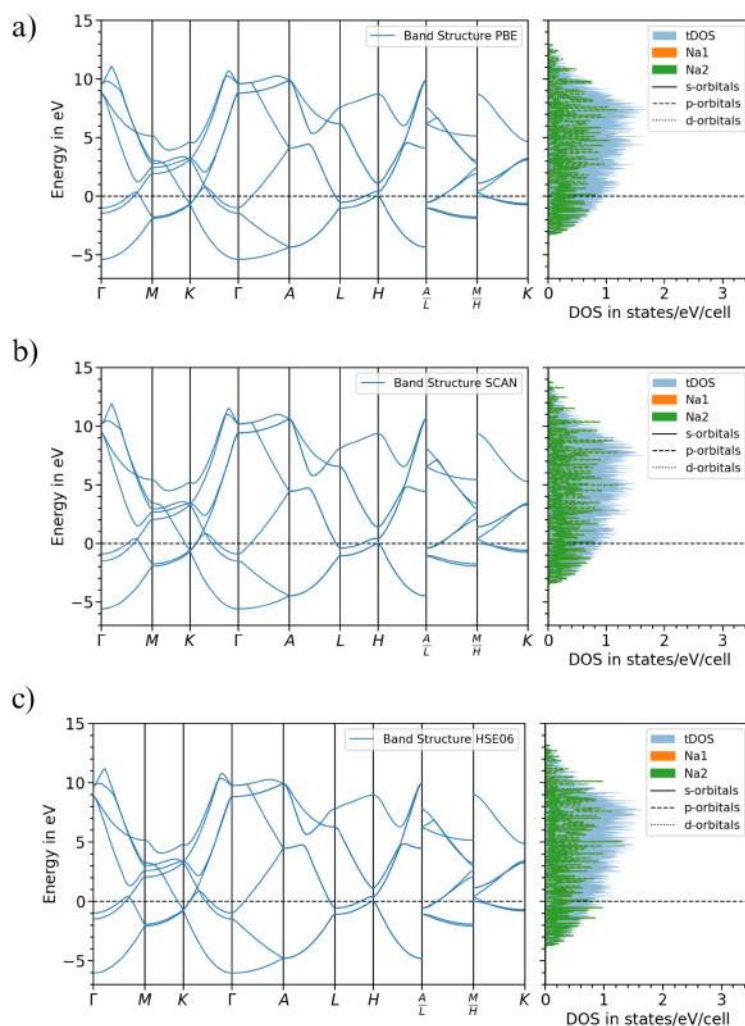


FIGURE 6.1: Na's band structure and PDOS were obtained using different functionals: PBE, SCAN, and HSE06. The energy is referenced to the valence band maximum (dashed line).

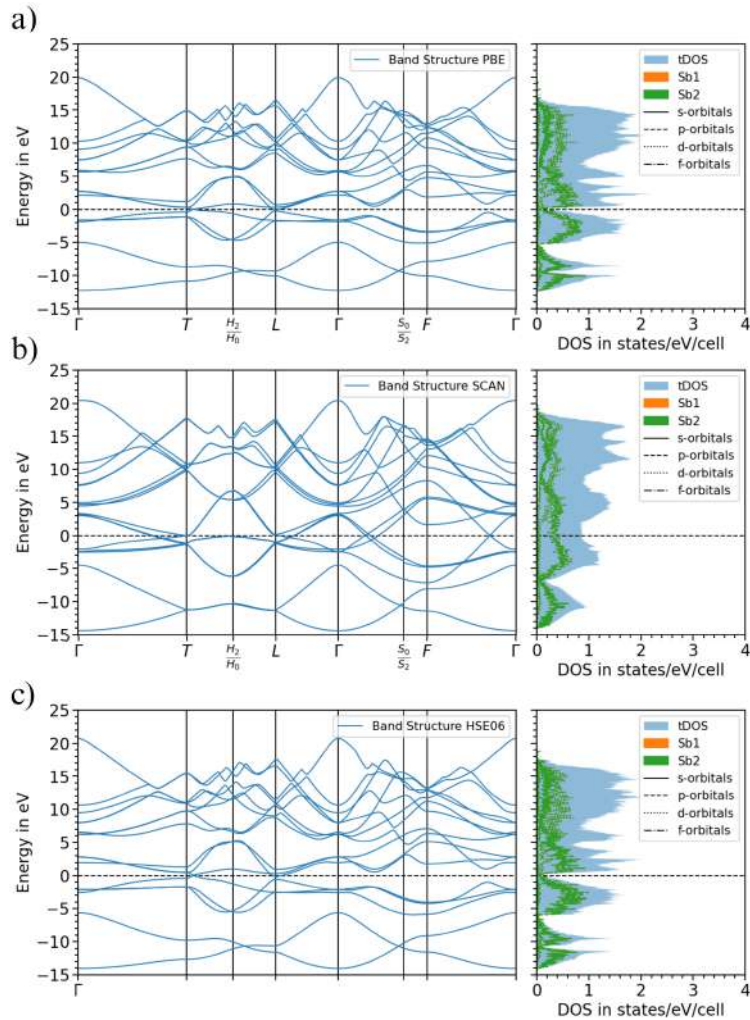


FIGURE 6.2: Comparison of Sb's band structure and PDOS using three different functional methods: PBE, SCAN, and HSE06. The valence band maximum is marked as the zero energy level with a dashed line.

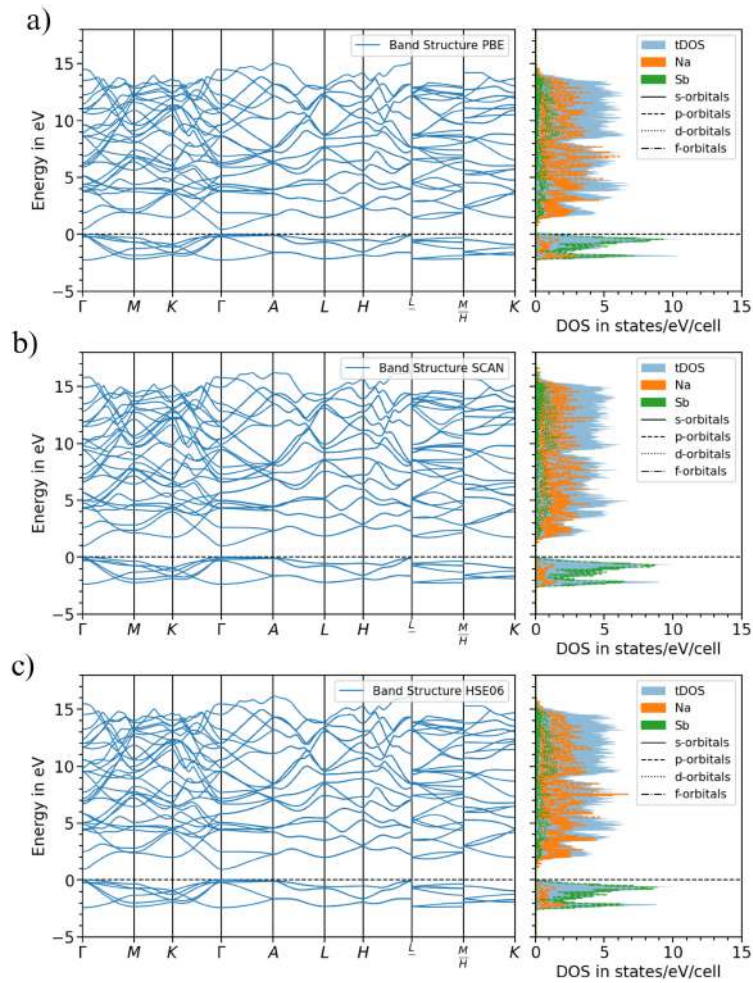


FIGURE 6.3: The band structure and partial density of states (PDOS) of Na_3Sb were determined using three different functional methods: PBE, SCAN, and HSE06. The zero energy level is marked by a dashed line, representing the valence band maximum. The contribution from various orbitals (s, p, d, and f) is depicted by solid, dashed, dotted, and dash-dotted lines, respectively.

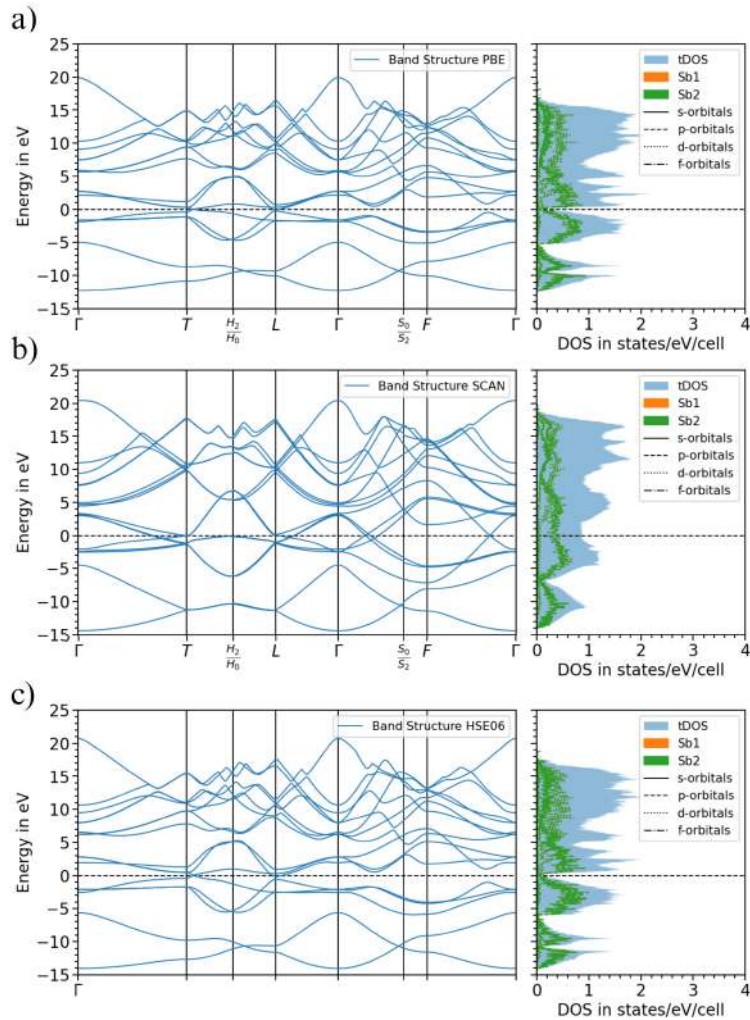


FIGURE 6.4: Comparison of Sb's band structure and PDOS using three different functional methods: PBE, SCAN, and HSE06. The valence band maximum is marked as the zero energy level with a dashed line.

Bibliography

- (1) Cultrera, L.; Rocco, E.; Shahedipour-Sandvik, F.; Bell, L. D.; Bae, J. K.; Bazarov, I. V.; Saha, P.; Karkare, S.; Arjunan, A. *Journal of Applied Physics* **2022**, *131*, DOI: 10.1063/5.0076488.
- (2) Schubert, S.; Ruiz-Osés, M.; Ben-Zvi, I.; Kamps, T.; Liang, X.; Muller, E.; Müller, K.; Padmore, H.; Rao, T.; Tong, X.; Vecchione, T.; Smedley, J. *APL Materials* **2013**, *1*, DOI: 10.1063/1.4821625.
- (3) Dowell, D. H.; Bazarov, I.; Dunham, B.; Harkay, K.; Hernandez-Garcia, C.; Legg, R.; Padmore, H.; Rao, T.; Smedley, J.; Wan., W. *Nuclear Instruments and Methods in Physics Research, Section A: Accelerators, Spectrometers, Detectors and Associated Equipment* **2010**, *622*, 685–697.
- (4) Antoniuk, E. R.; Schindler, P.; Schroeder, W. A.; Dunham, B.; Pianetta, P.; Vecchione, T.; Reed, E. J. *Advanced Materials* **2021**, *33*, DOI: 10.1002/adma.202104081.
- (5) Spicer, W. E., DOI: 10.1103/PhysRev.112.114.
- (6) Musumeci, P.; Navarro, J. G.; Rosenzweig, J. B.; Cultrera, L.; Bazarov, I.; Maxson, J.; Karkare, S.; Padmore, H. *Nuclear Instruments and Methods in Physics Research, Section A: Accelerators, Spectrometers, Detectors and Associated Equipment* **2018**, *907*, 209–220.
- (7) Perdew, J. P.; Sun, J.; Martin, R. M.; Delley, B. *International Journal of Quantum Chemistry* **2016**, *116*, 847–851.
- (8) Sholl, D. S.; Steckel, J. A., *Density Functional Theory: A Practical Introduction*, 2009.
- (9) Giustino Feliciano doi = 10.1080/00107514.2015.1100218, i. i. j. C. t. M. v. y.
- (10) Galsin, J. S., *Solid State Physics: An Introduction to Theory*, 2019.
- (11) Groß, A., *Theoretical Surface Science*, 2009.
- (12) Mardirossian, N.; Head-Gordon, M. *Molecular Physics* **2017**, *115*, 2315–2372.
- (13) *Mathematical Physics in Theoretical Chemistry* **2018**, DOI: 10.1016/B978-0-12-813651-5.10000-2.
- (14) Jensen, E.; Plummer, E. W. *Physical Review Letters* **1985**, *55*, 1912.

- (15) Perdew, J. P.; Burke, K.; Ernzerhof, M. **1996**.
- (16) Kohn, W.; Sham, L. J. *Physical Review* **1965**, *140*, DOI: 10.1103/PhysRev.140.A1133.
- (17) Perdew, J. P.; Ruzsinszky, A.; Tao, J.; Staroverov, V. N.; Scuseria, G. E.; Csonka, G. I. *Journal of Chemical Physics* **2005**, *123*, DOI: 10.1063/1.1904565/932647.
- (18) Perdew, J. P.; Yue, W. *Physical Review B* **1986**, *33*, DOI: 10.1103/PhysRevB.33.8800.
- (19) Hammer, B.; Hansen, L. B.; Nørskov, J. K. *Physical Review B - Condensed Matter and Materials Physics* **1999**, *59*, DOI: 10.1103/PhysRevB.59.7413.
- (20) Becke, A. D. *Physical Review A* **1988**, *38*, DOI: 10.1103/PhysRevA.38.3098.
- (21) Becke, A. D. *Journal of Computational Chemistry* **1999**, *20*, DOI: 10.1002/(SICI)1096-987X(19990115)20:1<63::AID-JCC8>3.0.CO;2-A.
- (22) Schimka, L.; Harl, J.; Kresse, G. *Journal of Chemical Physics* **2011**, *134*, DOI: 10.1063/1.3524336.
- (23) Zhang, Y.; Kitchaev, D. A.; Yang, J.; Chen, T.; Dacek, S. T.; Sarmiento-Pérez, R. A.; Marques, M. A.; Peng, H.; Ceder, G.; Perdew, J. P.; Sun, J. *npj Computational Materials* **2018**, *4*, DOI: 10.1038/s41524-018-0065-z.
- (24) Zhang, Y.; Kitchaev, D. A.; Yang, J.; Chen, T.; Dacek, S. T.; Sarmiento-Pérez, R. A.; Marques, M. A.; Peng, H.; Ceder, G.; Perdew, J. P.; Sun, J. *npj Computational Materials* **2018**, *4*, DOI: 10.1038/s41524-018-0065-z.
- (25) Zhang, G. X.; Reilly, A. M.; Tkatchenko, A.; Scheffler, M. *New Journal of Physics* **2018**, *20*, DOI: 10.1088/1367-2630/aac7f0.
- (26) Becke, A. D. *The Journal of Chemical Physics* **1993**, *98*, DOI: 10.1063/1.464304.
- (27) Becke, A. D. *The Journal of Chemical Physics* **1993**, *98*, DOI: 10.1063/1.464913.
- (28) *Materials Today* **2003**, *6*, DOI: 10.1016/s1369-7021(03)01229-x.
- (29) Schaber, J.; Xiang, R.; Gaponik, N. *Journal of Materials Chemistry C* **2023**, *11*, 3162–3179.
- (30) Schaber, J.; Xiang, R.; Teichert, J.; Arnold, A.; Murcek, P.; Zwartek, P.; Ryzhov, A.; Ma, S.; Gatzmaga, S.; Michel, P.; Gaponik, N. *Micromachines* **2022**, *13*, DOI: 10.3390/mi13060849.
- (31) Spicer, W.; Herrera-Gomez, A *SPIE* **1993**, *18*.
- (32) Schoenlein, R.; Elsaesser, T.; Holldack, K.; Huang, Z.; Kapteyn, H.; Murnane, M.; Woerner, M. *Philosophical Transactions of the Royal Society A: Mathematical, Physical and Engineering Sciences* **2019**, *377*, DOI: 10.1098/rsta.2018.0384.

- (33) Hernandez-Garcia, C.; Stutzman, M. L.; O'Shea, P. G. *Physics Today* **2008**, *61*, 44–49.
- (34) Wei, S.-H.; Zunger, A. *PHYSICAL REVIEW*, *8*, 15–1987.
- (35) Bazarov, I. V.; Dunham, B. M.; Sinclair, C. K. *Physical Review Letters* **2009**, *102*, DOI: 10.1103/PhysRevLett.102.104801.
- (36) Karkare, S.; Boulet, L.; Cultrera, L.; Dunham, B.; Liu, X.; Schaff, W.; Bazarov, I. *Physical Review Letters* **2014**, *112*, DOI: 10.1103/PhysRevLett.112.097601.
- (37) Erjavec, B **1994**.
- (38) Saha, P.; Chubenko, O.; Gevorkyan, G. S.; Kachwala, A.; Knill, C. J.; Sarabia-Cardenas, C.; Montgomery, E.; Poddar, S.; Paul, J. T.; Hennig, R. G.; Padmore, H. A.; Karkare, S. *Applied Physics Letters* **2022**, *120*, DOI: 10.1063/5.0088306.
- (39) Nangoi, J. K. **2022**.
- (40) Li, W. H.; Duncan, C. J.; Andorf, M. B.; Bartnik, A. C.; Bianco, E.; Cultrera, L.; Galdi, A.; Gordon, M.; Kaemingk, M.; Pennington, C. A.; Kourkoutis, L. F.; Bazarov, I. V.; Maxson, J. M. *Structural Dynamics* **2022**, *9*, DOI: 10.1063/4.0000138.
- (41) Parzyck, C. T.; Galdi, A.; Nangoi, J. K.; DeBenedetti, W. J. I.; Balajka, J.; Faeth, B. D.; Paik, H.; Hu, C.; Arias, T. A.; Hines, M. A.; Schlom, D. G.; Shen, K. M.; Maxson, J. M. **2021**, DOI: 10.1103/PhysRevLett.128.114801.
- (42) Wei, S.-H.; Zunger, A. *PHYSICAL REVIEW*, *8*, 15–1987.
- (43) Tubes, H. P. K. P. *Electron Tubes Division* **2006**, DOI: https://www.hamamatsu.com/content/dam/hamamatsuphotonics/sites/documents/99_SALES_LIBRARY/etd/PMT_handbook_v4E.pdf.
- (44) Wang, E. et al. *Scientific Reports* **2021**, *11*, DOI: 10.1038/s41598-021-83997-1.
- (45) Guo, L.; Kuriki, M.; Yokota, A.; Urano, M.; Negishi, K. *Progress of Theoretical and Experimental Physics* **2017**, *2017*, DOI: 10.1093/ptep/ptx030.
- (46) Honda, Y.; Matsuba, S.; Jin, X.; Miyajima, T.; Yamamoto, M.; Uchiyama, T.; Kuwahara, M.; Takeda, Y. *Japanese Journal of Applied Physics* **2013**, *52*, DOI: 10.7567/JJAP.52.086401.
- (47) Guo, T. *Thin Solid Films* **1996**, *281-282*, 379–382.
- (48) Vecchione, T.; Ben-Zvi, I.; Dowell, D. H.; Feng, J.; Rao, T.; Smedley, J.; Wan, W.; Padmore, H. A. *Applied Physics Letters* **2011**, *99*, DOI: 10.1063/1.3612916.
- (49) Dolizy, P.; Grolière, F.; Lemonier, M. *Advances in Electronics and Electron Physics* **1988**, *74*, 331–338.

-
- (50) Michelato, P.; Bona, A. D.; Pagani, C.; Sertore, D.; Valeri, S. In 1995; Vol. 2.
- (51) Blum, V.; Rossi, M.; Kokott, S.; Scheffler, M.
- (52) Galadanci, G. S. M.; Babaji, G. *IOSR Journal of Applied Physics (IOSR-JAP)*, 4, 85–95.
- (53) Blum, V.; Gehrke, R.; Hanke, F.; Havu, P.; Havu, V.; Ren, X.; Reuter, K.; Scheffler, M. *Computer Physics Communications* **2009**, 180, 2175–2196.
- (54) Abdu, S. G.; Shu', A.; Aboh, M.; Abubakar, M. S. *Science World Journal*, 14, 2019.
- (55) Bahn, S. R.; Jacobsen, K. W. *Comput. Sci. Eng.* **2002**, 4, 56–66.
- (56) Larsen, A. H. et al. *Journal of Physics: Condensed Matter* **2017**, 29, 273002.
- (57) Hinuma, Y.; Pizzi, G.; Kumagai, Y.; Oba, F.; Tanaka, I. *Computational Materials Science* **2017**, 128, 140–184.
- (58) Togo, A.; Shinohara, K.; Tanaka, I. Spglib: a software library for crystal symmetry search, 2024.
- (59) Kresse, G; Furthmü, J **1996**.
- (60) Tran, F.; Stelzl, J.; Blaha, P. *Journal of Chemical Physics* **2016**, 144, DOI: 10.1063/1.4948636.
- (61) Saïsnick, H. D.; Cocchi, C. *Electronic Structure* **2021**, 3, DOI: 10.1088/2516-1075/abfb08.
- (62) Kahn, A. *Materials Horizons* **2016**, 3, 7–10.
- (63) Ichi Chikawa, J.; Imamura, S. *Journal of the Physical Society of Japan* **1961**, 16, DOI: 10.1039/c5mh00160a.
- (64) Ettema, A. R. H. F.; Groot, R. A. D. *Physical Review* **1999**, 61.
- (65) Rgzet, M; Hafnert, J I. *Phys.: Condens. Matter* **1992**, 4, 2449–2474.
- (66) Sangster, J; Pelton, A. D.
- (67) Hybertsen, M. S.; Louie, S. G.; Eq, S.; El, S. **1985**, 55.
- (68) Brodersen, S.; Lukas, D.; Schattke, W. *Physical Review B - Condensed Matter and Materials Physics* **2002**, 66, 1–8.
- (69) Wisert, N. *PHYSICAL REVIEW VOIRUME* **1963**, 129.
- (70) Sole, R. D.; Vergata, T.; via della Ricerca Scientigca; Girlanda, I. R. *PHYSICAL REVIEW B*, 48, 15–1993.
- (71) Ambrosch-Draxl, C.; Sofo, J. O. *Computer Physics Communications* **2006**, 175, 1–14.

- (72) Sole, R. D.; Vergata, T.; via della Ricerca Scientifica; Girlanda, I. R. *PHYSICAL REVIEW B*, **48**, 15–1993.
- (73) Puschnig, P.; Ambrosch-Draxl, C. *Advanced Engineering Materials* **2006**, *8*, 1151–1155.
- (74) Ambrosch-Draxl, C.; Sofo, J. O. *Computer Physics Communications* **2006**, *175*, 1–14.
- (75) Vorwerk, C.; Cocchi, C.; Draxl, C. *Physical Review B* **2017**, *95*, DOI: 10.1103/PhysRevB.95.155121.
- (76) Browne, A. J.; Krajewska, A.; Gibbs, A. S. *Journal of Materials Chemistry C* **2021**, *9*, 11640–11654.
- (77) Streltsov, S. V.; Khomskii, D. I. *Physical Review X* **2020**, *10*, DOI: 10.1103/PhysRevX.10.031043.
- (78) Dunn, T. M.
- (79) Khomskii, D. I.; Streltsov, S. V. *Chemical Reviews* **2021**, *121*, 2992–3030.
- (80) Allan, P. K.; Griffin, J. M.; Darwiche, A.; Borkiewicz, O. J.; Wiaderek, K. M.; Chapman, K. W.; Morris, A. J.; Chupas, P. J.; Monconduit, L.; Grey, C. P. *Journal of the American Chemical Society* **2016**, *138*, 2352–2365.
- (81) Caputo, R. *Journal of Electronic Materials* **2016**, *45*, 999–1010.
- (82) Kokalj, A. **2000**.
- (83) Ebina, K. A.; Takahashi, T. *Zh. Eksp. Teor. Fiz. Pis'ma Red* **1973**, *21*, 4712–4719.
- (84) Mecarroll, W. H. *J. Phys. Chem. Solids Pergamon Press* **1960**, *16*, 30–36.
- (85) Sangster, J.; Pelton, A. D.
- (86) Scheer, J. J.; Zalm, P. C. In 2014.
- (87) Sommer, A. *Nature* **1941**, *148*.
- (88) Liu, H.; Bai, X.; Ning, J.; Hou, Y.; Song, Z.; Ramasamy, A.; Zhang, R.; Li, Y.; Sun, J.; Xiao, B. *The Journal of Chemical Physics* **2024**, *160*, DOI: 10.1063/5.0176415.
- (89) Zhou, W.; Zhang, S.; Guo, S.; Qu, H.; Cai, B.; Chen, X.; Zeng, H. *Nanoscale* **2020**, *12*, 18931–18937.
- (90) Jain, A.; Ong, S. P.; Hautier, G.; Chen, W.; Richards, W. D.; Dacek, S.; Cholia, S.; Gunter, D.; Skinner, D.; Ceder, G.; Persson, K. a. *APL Materials* **2013**, *1*, 011002.
- (91) Amador, R.; Saßnick, H. D.; Cocchi, C. *Journal of Physics Condensed Matter* **2021**, *33*, DOI: 10.1088/1361-648X/ac0e70.

-
- (92) Cocchi, C.; Mistry, S.; Schmeißer, M.; Amador, R.; Kühn, J.; Kamps, T. *Scientific Reports* **2019**, *9*, DOI: 10.1038/s41598-019-54419-0.
- (93) Kalarasse, L.; Bennecer, B.; Kalarasse, F. *Journal of Physics and Chemistry of Solids* **2010**, *71*, 314–322.